Numerical Analysis on the Generation, Propagation and Interaction of Solitary Waves

by a Harmonic Polynomial Cell Method

Chao Tong[1,2] , Yanlin Shao[4], Finn-Christian W. Hanssen[5] ,Ye Li[1,2,3,*]

1. School of Naval Architecture, Ocean & Civil Engineering, Shanghai Jiao Tong University, Shanghai, 200240, China
2. Collaborative Innovation Center for Advanced Ship and Deep-Sea Exploration, Shanghai Jiao Tong University, Shanghai 200240, China
3. Key Laboratory of the Ministry of Education, Shanghai Jiao Tong University, Shanghai 200240, China
4. Department of Mechanical Engineering, Technical University of Denmark
5. Centre for Autonomous Marine Operations and Systems (AMOS), Norwegian University of Science and Technology

Abstract

A numerical wave tank based on the Harmonic Polynomial Cell (HPC) method is created to study the generation, propagation and interaction of solitary waves. The HPC method has been proven to be of high accuracy and efficiency in modelling of water waves, wave-wave and wave-structure interaction within the context of potential flow. An important feature of the present HPC method is that the free surface and solid boundaries are immersed in a stationary Cartesian grid. Solitary waves with σ , i.e. amplitude to water depth ratio, up to 0.6 are generated by different methods. We demonstrate that the results based on the first-, third- and ninth-order method are less satisfactory than the fully-nonlinear method in generating solitary waves with $\sigma > 0.4$. Additionally, both the head-on and overtaking collision between two solitary waves are studied. In the investigation of the phase shifts after the head-on collision, our window model successfully explain the main reason why Su & Mirie [1]'s third-order approximation of the uniform phase shifts is inconsistent with Chen & Yeh's [2] experimental results and Craig *et al.*'s [3] fully nonlinear numerical results. For the overtaking collision of solitary waves, the collision process and the phase shifts are numerically analyzed. Our present result also confirms Craig *et al.*'s [3] category of the overtaking collision.

Keywords: solitary wave; wave generation; wave propagation; wave interaction; Harmonic Polynomial Cell method.

1. Introduction

Since discovered by Scott Russell [4], solitary waves have played an important role in modelling tsunamis near the shore. In order to better understand the mechanism of solitary waves, there have been considerable studies on their behaviors. Among these researches, the essential aspect is how to generate solitary waves accurately. There exist various methods of solitary wave generation in wave flumes [5-11], among which the piston-type wave maker is the most commonly used in experiments. Considering that the prescribed velocity of the wave paddle shall equal the uniform horizontal velocity of the water particles on the wave maker boundary, Goring [8] derived the motion of a piston-type wave maker. By applying Boussinesq's [12] solitary wave solution, Goring's method has been primarily used in experiments to study solitary waves in the last decades [13-15]. However, it was observed by Grilli & Svendsen [16] in a numerical study that Goring's method only performed well for solitary waves of smaller amplitude, but the amplitude of a generated solitary wave was slightly smaller than the desired value and attenuated continuously during propagation for higher waves, in spite of neglecting water viscosity. In order to generate solitary waves as accurate as possible, Katell & Eric [9] carried out experiments to generate solitary waves by using a paddle motion law from Rayleigh [17], and they observed that the features of generated waves were in close agreement with those of desired ones. However, Wu *et al.* [18] pointed out that the boundary outskirt decay coefficient used in Katell & Eric [9] was smaller than the value based on Boussinesq's [12] solution. More water volume has been consequently pushed forward so that the wave amplitude was higher than the designed value in their numerical study. Having noticed the transient behaviors of solitary waves adjacent to the wave paddle in the process of wave generation, Malek-Mohammadi & Testik [10] proposed a new methodology by assuming that the wave speed is time-dependent at the wave paddle during wave generation. They concluded that solitary waves generated through their methodology were less dispersive to retain a permanent form. Based

on Goring's paddle movement formula, Wu *et al.* [18] carried out numerical experiments by using different solitary wave solutions. They found that Goring's formula using the ninth-order solution of Fenton [19] could extend the applicability of Goring's method to a relative higher wave amplitude. Therefore, a modified Goring's method was proposed and laboratorial experiments were also carried out later by Wu *et al.* [11] in a water flume to validate the modified Goring's method.

It is known that the maximum run-up during a head-on collision of two solitary waves is higher than the sum of their initial wave amplitudes [20]. Maxworthy [21] carried out experiments to investigate the run-up and the phase shifts after the head-on collision of two identical solitary waves. It was confirmed that the wave profile reached a maximum run-up greater than twice the initial wave amplitude and both waves suffered a time delay after the interaction. Su & Mirie [1] proposed a third-order perturbation method to analyze the head-on collision of two arbitrary-amplitude solitary waves and obtained the solutions for maximum run-up, phase shifts and the secondary trailing waves. In a later numerical analysis, Mirie & Su [22] found that solitary waves lost energy to the trailing waves causing reduction of wave amplitude. Fenton & Rienecker [23] numerically studied the head-on collision based on Fourier series. They pointed out that although the maximum run-up was consistent with Su & Mirie's [1] third-order approximation and Chan & Street's [24] numerical result, the third-order theory seemed unable to predict the phase shifts. The measurement of the phase shifts is strongly dependent on the measurement location due to the change of the wave speed after the interaction. Renouard *et al.* [25] in their experiments observed an amplitude decay after the reflection of a solitary wave from a vertical wall. The wave reflection was also investigated by Cooker *et al.* [26]. They discovered that both amplitude and energy loss occur after the reflection due to the dispersive trailing wavetrain. It was also found that the run-up process was shorter than the run-down process. In other words, the asymmetry of the process could have resulted in the observed trailing waves. Craig *et al.* [3] systematically studied the head-on collision and overtaking collision of two solitary waves by solving the Euler equations for water-wave problems. They analyzed the residual produced by the wave-wave interaction and estimated the energy carried away by the trailing waves. Laboratorial experiments on the head-on collision of two solitary waves were carried out by Chen & Yeh [2] using the laser induced fluorescence (LIF) technique with a montage method to provide precise measurement of free surface profile. Chen *et al.* [27] also showed detailed flow fields on velocity, acceleration, vorticity and velocity-gradient tensor related to the head-on collision.

For the overtaking collision of two different solitary waves, Lax [28] theoretically proposed a category of the KdV overtaking interaction based on the amplitude ratio of the two solitary waves. The same notation was also employed in the experiments of Weidman & Maxworthy [29]. Zabusky & Kruskal [30] simulated a large solitary wave overtaking a smaller one and found that the solitary waves retained their initial shapes after the interaction except for a spatial phase change. Mirie & Su [22] observed that the trailing waves behind the smaller wave after the interaction are much smaller than those in a head-on collision. Fenton & Rienecker [23] carried out a simulation of an overtaking collision of two solitary waves with amplitude ratio of 3.142 and found that the category proposed by Lax [28] was not able to explain their numerical results. Similar discrepancy was also observed by Craig *et al.* [3] in their numerical and experimental study. Hence, a modification of Lax's [28] category has been proposed by Craig *et al.* [3]. Fenton & Rienecker [23] and Craig *et al.* [3] also discovered that the higher wave would slightly grow in amplitude but the opposite for the smaller one after the interaction. Gardner *et al.* [31] showed that the overtaking collision between two solitary waves were elastic, where the term 'elastic' means that solitary waves will regain their wave form and velocity except for phase shift after the collision. Sachs [32] showed that overtaking collision of solitary waves was elastic up to the second-order approximation. Zou & Su [33] obtained second- and third-order approximation of water wave equations based on the first-order KdV equation and confirmed that the overtaking collision was elastic up to second order approximation. Their third-order numerical results were also able to explain the dispersive trailing waves behind the smaller solitary wave after the interaction.

There exist many different numerical methods that can model solitary waves in the literature. It has been a strong tradition to use the Boundary Element Method [34,35] to model the fully-nonlinear water waves in the frame of potential flow. However, the bottleneck of the conventional Boundary Element Method is that both CPU time and computer memory requirement increase quadratically with the number of unknowns. Under this circumstances, Shao & Faltinsen [36] newly proposed a potential-flow field solver named the HPC method, which has been proven to be highly efficient and accurate for 2D fully-nonlinear potential flow problems. Lately the HPC method was extended to 3D by Shao & Faltinsen [37] and it was also demonstrated to be of high efficiency and accuracy in some marine applications, such as liquid sloshing in tanks, nonlinear wave diffraction and wave propagation over various topographies. Additionally, the HPC method has been advanced in many

aspects in recent years. Fredriksen *et al.* [38] coupled a Navier-Stokes solver with the HPC method to study the water behavior in the moonpool of a ship. Liang *et al.* [39] used the HPC method along with a domain decomposition strategy to treat the singular flow at sharp corners. They also solved lifting problems of a hydrofoil by using a double-layer nodes technique. Zhu *et al.* [40] and Hanssen *et al.* [45] applied an immersed free surface strategy to the 2D HPC method. Hanssen *et al.* [41] created a nonlinear numerical wave tank by the 2D HPC method, adopting two strategies to track the free surface, i.e. immersed boundary (IB) and multigrid. Ma *et al.* [42] gave a detailed and systematic analysis on the local and global properties of the 2D HPC method. After a comparison of various gridding strategies, they concluded that the grid refinement with square-shaped cells was highly recommended due to the minimum local error in numerical calculations. Bardazzi *et al* [43] extended the original 3D method to a generalized HPC method, which was confirmed the 4th order accuracy when the method was applied in solving Poisson equation and even in dealing with cases with singular solutions. Wang & Faltinsen [44] applied Cartesian grids with an adaptive local refinement in the HPC method to accurately represent the highly-deformed free surface boundary and complicated body geometries. The method makes it possible to solve highly-nonlinear wave-wave and wave-structure interaction problems, e.g. the plunging breakers and water entry of solid objects, very accurately and efficiently.

In the present study, a fully-nonlinear wave tank is created by the 2D HPC method. The free surface, which is treated as an immersed boundary in a structured Cartesian grid, is tracked by a set of markers moving only in vertical direction.

The paper is organized as follows: In Section 2 we give an introduction the present 2D HPC method and the treatments of free surface conditions in both the background grid and the wave-maker grid. In Section 3, after we compare the numerically generated solitary waves by using different solutions, validation of the numerical results against laboratorial experiments is also presented. In Section 4, the head-on collision of solitary waves is investigated with the focus on the phase shifts after the interaction. Additionally, the overtaking collision is also studied and the category of the overtaking interaction is discussed.

2. Mathematical consideration

2.1 2D Harmonic Polynomial Cell method

A numerical water wave tank is defined and the origin of a global Cartesian coordinate system with axes (x, z) is located at the midpoint of the tank, on the mean water level. A local body-fixed coordinate system $x'O'z'$ with the origin at the bottom of the wave paddle is also introduced, which is applied in the wave maker fixed reference frame in Sec. 2.3. A sketch of the wave tank and the coordinate systems are given in **Figure. 1**.
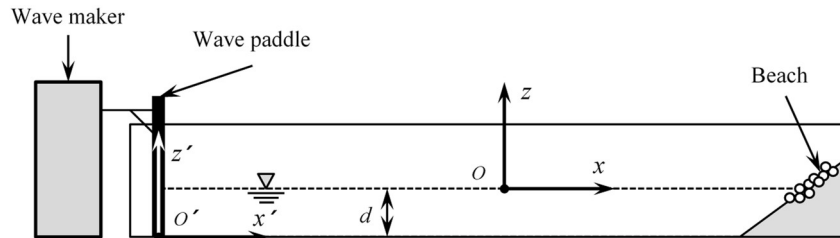

Figure 1. Sketch of a 2D water wave tank with a piston-type generator. Both the global coordinate system xOz and the local body-fixed coordinate system $x'O'z'$ are introduced.

The fluid is assumed to be incompressible, inviscid, and the flow is irrotational, which can be described by the Laplace equation:

$$\Delta \varphi (x, z) = 0 . \tag{1}$$

The whole computational domain can be discretized by quadrilateral overlapping cells as shown in **Figure. 2**. Each cell consists of eight boundary nodes with local indices 1-8 and a central node with local index 9. We introduce a local cell coordinate system with the origin at the central node, namely,

$$\begin{cases} \zeta = x - x_9, \\ \xi = z - z_9, \end{cases} \tag{2}$$

where (x, z) are global coordinates and (x_9, z_9) are the global coordinates of the central node.
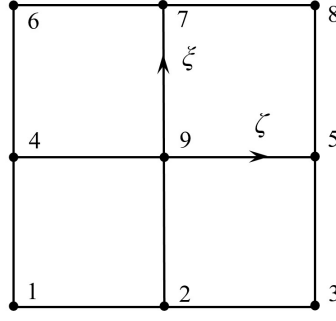
Figure 2. Sketch of a cell with local node indices and the local cell coordinate system.

According to Shao & Faltinsen [36], the velocity potential φ at an arbitrary location within a cell can be approximated by the linear superposition of velocity potential φ_i of the eight boundary nodes

$$\varphi(\zeta,\xi) = \sum_{i=1}^{8}\left[\sum_{j=1}^{8} c_{j,i} f_j(\zeta,\xi)\right]\varphi_i. \tag{3}$$

Here $f_j(\zeta,\xi)$ are the eight harmonic polynomials given by Shao & Faltinsen [36]: $f_1(\zeta,\xi)=1$; $f_2(\zeta,\xi)=\zeta$; $f_3(\zeta,\xi)=\xi$; $f_4(\zeta,\xi)=\zeta^2-\xi^2$; $f_5(\zeta,\xi)=\zeta\xi$; $f_6(\zeta,\xi)=\zeta^3-3\zeta\xi^2$; $f_7(\zeta,\xi)=3\zeta^2\xi-\xi^3$; $f_8(\zeta,\xi)=\zeta^4-6\zeta^2\xi^2+\xi^4$, where $c_{j,i}$ are elements of the inverse of the matrix $[\mathbf{D}]$ whose elements are $d_{j,i}=f_j(\zeta_i,\xi_i)$. Since all these harmonic polynomials satisfy the Laplace equation everywhere in the fluid domain, the velocity potential described in **Eq. (3)** automatically satisfies the Laplace equation.

The velocity potential of the 9$^{\text{th}}$ node in each cell can be further simplified as

$$\varphi_9 = \varphi(\zeta_9=0,\xi_9=0) = \sum_{i=1}^{8} c_{1,i}\varphi_i. \tag{4}$$

This equation serves as a connectivity equation employed for every node in the fluid domain (except for nodes along the boundaries of the numerical wave tank), because each of them will be the central node of a particular cell. For grid nodes in the fluid, it is straightforward to impose continuity of velocity potential in the fluid by **Eq. (4)**. For points in the domain that do not coincident with grid nodes, the velocity potential can be directly approximated by using **Eq. (3)** with local coordinate (ζ_p,ξ_p) in an appropriately chosen cell. For nodes along a Neumann boundary, the Neumann boundary conditions are fulfilled by taking the normal derivative of **Eq. (3)**

$$\frac{\partial\varphi}{\partial n}(\zeta,\xi) = \sum_{i=1}^{8}\left[\sum_{j=1}^{8} c_{j,i}\nabla f_j(\zeta,\xi)\cdot\bar{n}(\zeta,\xi)\right]\varphi_i, \tag{5}$$

where $\bar{n}(\zeta,\xi)$ is the unit normal vector of the Neumann boundary at the node (ζ,ξ).

2.2 Free surface boundary conditions in the background grid

In our study, an Immersed Boundary (IB) method is used to handle the free surface conditions. The IB method was primarily combined with the 2D HPC method by Hanssen *et al.* [45] to impose body-boundary conditions on a solid body in an exterior flow. The method along with a free-surface tracking strategy was later used for imposing Dirichlet-type free-surface conditions in a fully nonlinear water wave tank [41]. In our numerical experiments, the free surface is assumed to be calm at $t=0$s. We technically represent the free surface by a set of markers, which are evenly distributed in horizontal direction. As illustrated in **Figure. 3**, the free-surface markers are only allowed to move freely along the vertical grid lines in the background Cartesian gird, so that the wave elevation is assumed as a single-value function. Each free-surface marker is restricted in the upper half area of the associated cell. The upper layer cells of the free surface are marked in gray in **Figure. 3**, which contain certain nodes above the free surface. Those nodes shall be considered as ghost nodes, whose velocity potentials are also unknown. Free surface conditions are enforced by applying **Eq. (3)** with local coordinates (ζ_m,ξ_m) of free surface markers. Since the grid refinement remain unchanged at any time step, the inverse of matrix $[\mathbf{D}]$ only needs to be determined once at the start of the simulation.
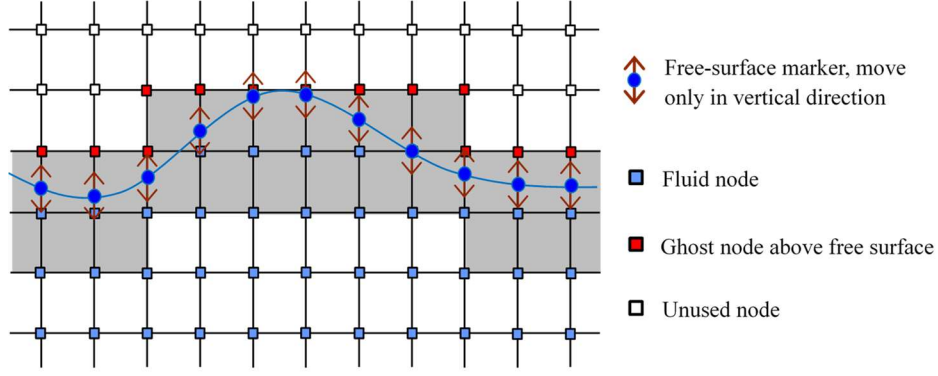
Figure 3. The free surface is treated as an immersed boundary in a structured background grid, which is tracked by free-surface markers moving vertically as indicated by arrows. The cells used to impose free-surface conditions on are filled with gray.

In order to satisfy the fully nonlinear free surface conditions, the semi-Lagrangian method is adopted to describe kinematic and dynamic free surface conditions for a vertically moving marker with global coordinates (x_m, z_m), namely

$$\frac{Dx_m}{Dt} = 0, \quad \frac{Dz_m}{Dt} = \frac{\partial \varphi}{\partial z} - \frac{\partial \varphi}{\partial x}\frac{\partial \eta}{\partial x} - \nu(x)\eta \; ; \tag{6}$$

$$\frac{D\varphi_m}{Dt} = \frac{\partial \varphi}{\partial t} + \frac{\partial \eta}{\partial t}\frac{\partial \varphi}{\partial z} - \nu(x)\varphi$$
$$= -\frac{1}{2}\left|\left(\frac{\partial \varphi}{\partial x}\right)^2 + \left(\frac{\partial \varphi}{\partial z}\right)^2\right| - g\eta + \frac{\partial \eta}{\partial t}\frac{\partial \varphi}{\partial z} - \nu(x)\varphi \; , \tag{7}$$

where $z = \eta(t, x)$ denotes the free surface elevation, g is the gravity acceleration and the term $\nu(x)$ is a damping coefficient that is used to absorb the energy of the waves at the end of the tank to minimize wave reflection from the downstream tank wall. More details of the damping zone and damping coefficients are referred in Greco [46] and Hanssen *et al.* [41]. In the study of the interaction and reflection of solitary waves, $\nu(x)$ is set to be zero. Here we have used the semi-Lagrangian derivative $D/Dt = \partial/\partial t + \bar{v}_m \cdot \nabla$, where $\bar{v}_m = (0, \partial z_m/\partial t)$. All spatial derivatives are calculated at the instantaneous position (x_m, z_m) of a marker. The wave slope $\partial \eta/\partial x$ is evaluated using a high-order finite difference scheme. We use an explicit fourth-order Runge-Kutta scheme in time domain to integrate the free surface conditions.

2.3 Free surface boundary conditions in the wave-maker grid

A physical piston-type wave maker is simulated by introducing a local body-fitted grid on the right side of the wave paddle. This local grid overlaps with the background Cartesian grid, as depicted in **Figure. 4**. This local grid also slides over the background grid as the paddle moves, which possesses its own set of free-surface markers.

As described previously for the background grid, the free surface markers are only allowed to move along vertical grid lines in the global coordinate system. Similarly, markers in the wave maker grid are also only allowed to move along the z' axis in the wave maker fixed reference frame. The corresponding semi-Lagrangian free surface conditions for a marker in this reference frame can be written as:

$$\frac{Dx'_m}{Dt} = 0, \quad \frac{Dz'_m}{Dt} = \frac{\partial z'_m}{\partial t} + \left(u'_{grid} - \frac{\partial \varphi}{\partial x'}\right)\frac{\partial \eta'}{\partial x'} \; ; \tag{8}$$

$$\frac{D\varphi_m}{Dt} = -\frac{1}{2}\left|\left(\frac{\partial \varphi}{\partial x'}\right)^2 + \left(\frac{\partial \varphi}{\partial z'}\right)^2\right| - g\eta' + u'_{grid}\frac{\partial \varphi}{\partial x'} + \left(w'_{grid} + \frac{\partial \eta'}{\partial t}\right)\frac{\partial \varphi}{\partial z'} . \tag{9}$$

u'_{grid} and w'_{grid} are the horizontal and vertical velocity components of the grid point at a position (x', z') related to the movement of the paddle. The detail of the derivation of Eq. (8) and (9) can be found in Hanssen *et al.* [41].
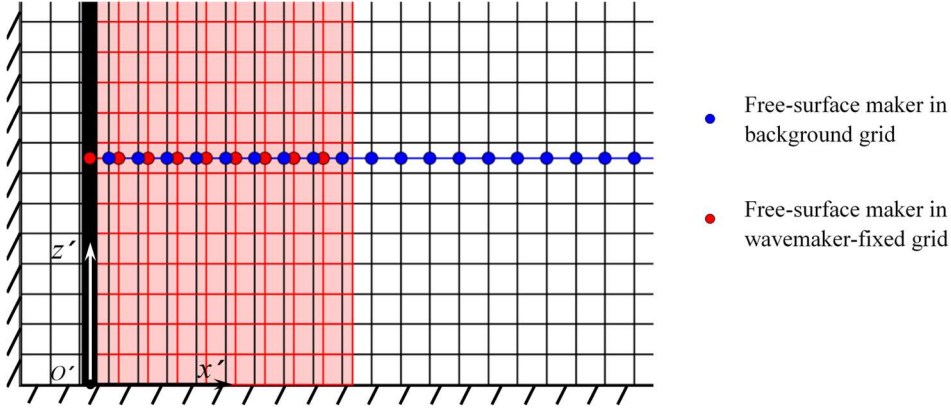
Figure 4. Modeling of the piston-type wave maker with structured body-fixed grid. The local grid fixed on the wave marker is marked in red while the background grid is marked in black.

By using overlapping grids, an important part is the exchange of information between the local wave-maker fitted grid and the background grid. The velocity potential of a grid point in the local grid can be interpolated from the background grid through:

$$\varphi_{WMG}(x',z') = \sum_{i=1}^{8}\left[\sum_{j=1}^{8}c_{j,i}f_j(\zeta,\xi)\right]\varphi_i\big|_{BGG}, \qquad (10)$$

where φ_{WMG} and φ_{BGG} are the velocity potential in the wave maker grid and in the background grid, respectively. Since in the fluid domain the velocity potential of a particular point is unique regardless of the selected reference frame, the velocity potential of a grid point (ζ,ξ) in the wave maker grid can be approximated by a cell in the background grid that contains the node (x',z'), i.e. by applying **Eq. (10)**. Correspondingly, nodes of the background grid in the overlapping region can also get the velocity potential from interpolation in the wave-maker fitted grid:

$$\varphi_{BGG}(x,z) = \sum_{i=1}^{8}\left[\sum_{j=1}^{8}c_{j,i}f_j(\zeta',\xi')\right]\varphi_i\big|_{WMG}. \qquad (11)$$

This ensures a direct two-way coupling between the regions in an implicit form.

All these boundary conditions together with **Eq. (4)** are combined to build a global linear algebraic matrix system for the velocity potential in the form of $[A]\{\varphi\}=\{b\}$. The coefficient matrix $[A]$ is sparse with at most 9 nonzero entities in each row so that the equations can be solved efficiently with standard solvers for sparse-matrix equations.

3. Validation and verification

The numerical water wave tank based on the HPC method presented in Section 2 will be verified and validated in this section through studies on solitary wave generation and head-on collision of two solitary waves.

3.1 Solitary wave generation

Piston-type wave makers have been widely used to generate solitary waves. Wu *et al.* [18] compared the solitary waves generated by applying Boussinesq's [12] first-order solitary wave solution, Rayleigh's [17] solution, Grimshaw's [47] third-order solution and Fenton's [19] ninth-order solution to Goring's [8] paddle motion formula. However, the use of Goring's formula is not compliance with the fluid particle velocity along the wave maker boundary, especially for highly nonlinear solitary waves. In that case, they were still unable to produce solitary waves of desired dimensionless amplitudes as $\sigma > 0.4$ ($\sigma = A/d$, d is the water depth).

In this part, we use Clamond & Dutykh's [48] fully nonlinear solitary wave solution as the wave maker boundary condition. The main difference between this method and Goring's method is that the wave maker is kept stationary in the process of generating waves. We only update fully nonlinear solution of the horizontal velocity along the wave maker boundary below the free surface, so that the method is named Fully Nonlinear (FNL) method.

Primarily, the numerical experiments of solitary wave generation are conducted to assess the convergence of the spatial

1 and temporal discretization for $\sigma = 0.4$ by the FNL method. The wave tank is set to be $L = 40$m, the tank height $H = 2$m and
2 the water depth $d = 1$m. **Table 1** gives the information of three grid refinements. ($\Delta x/d$, $\Delta z/d$) and (n_x, n_z) denote length and
3 number of grid elements in horizontal and vertical direction, respectively.
4
5 <center>**Table 1**. Grid refinements for the wave tank domain.</center>

Case	$\Delta x/d$	n_x	$\Delta z/d$	n_z
Coarse	0.20	200	0.20	10
Medium	0.10	400	0.10	20
Fine	0.0667	600	0.0667	30

6
7   According to Clamond & Dutykh's [48] fully nonlinear solution, the wave speed of the solitary wave is C = 3.6892m/s.
8 To make sure the *CFL* number ($CFL = C\Delta t / \Delta x$) below unity, the non-dimensional time step $\Delta \bar{t} = \Delta t \sqrt{g/d} = 0.01$ is used
9 for all simulations. **Figure 5** depicts the free surface at $\bar{t} = t\sqrt{g/d} = 37.579$ for the three grid refinements. The results obtained
10 here using the fine and medium mesh strategy are almost coincident while the amplitude cannot reach the target value for the
11 coarse mesh strategy. This indicates that the grid convergence is achieved using the medium grid refinement. Similar tests for
12 different time steps ($\Delta t = 0.01$s, 0.02s and 0.025s) using the medium grid refinement indicate that $\Delta t = 0.02$s is sufficient for
13 the accuracy.
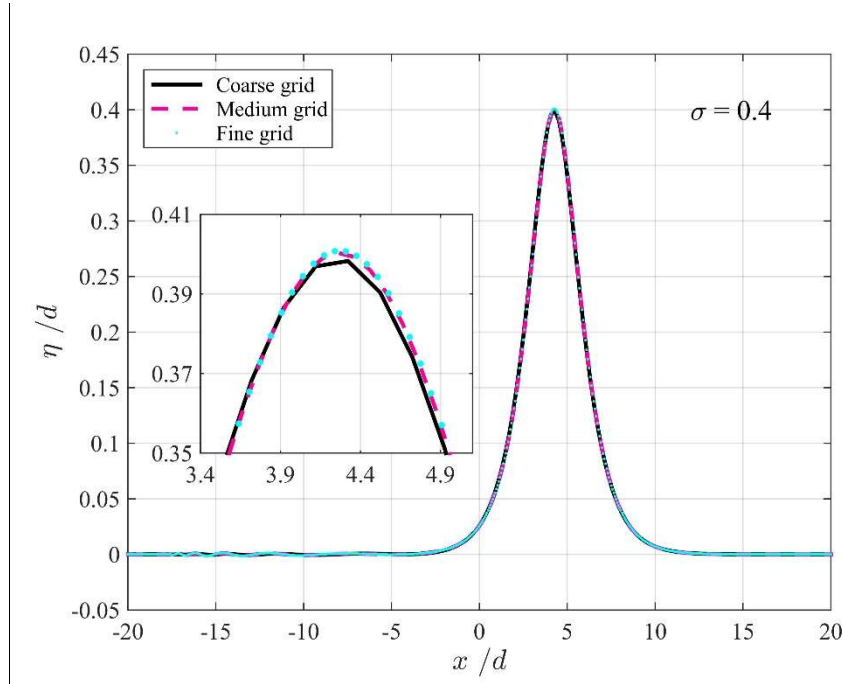

14
15 <center>**Figure 5**. Free surface profiles of solitary wave with $\sigma = 0.4$ for different grid refinements.</center>
16
17 <center>**Table 2**. The list of numerical conditions of cases for solitary wave generation.</center>

Method number	Method	Target wave amplitude σ
1	G1S	0.2 | 0.4 | 0.6
2	G3S	0.2 | 0.4 | 0.6
3	G9S	0.2 | 0.4 | 0.6
4	FLN	0.2 | 0.4 | 0.6

18
19   To conform the accuracy of this method, we compare numerical results of the FNL method with those of Goring's method
20 by using the first-, third-, and ninth-order solitary wave solution (Here, we call them G1S, G3S and G9S method for simplicity).
21 We have to remark that the wave maker is only kept still when applying the FNL method to produce solitary waves, but not
22 for Goring's method.
23   The height of the numerical wave tank is $H = 2$m, the length is $L = 80$m and the calm water depth is $d = 1$m. The whole

1 domain is horizontally and vertically discretized into 600 and 30 elements, respectively. A time step $\Delta t = 0.02$s is chosen in
2 this simulation. The conditions of the cases are listed in **Table 2**.

3   **Figure. 6(a)**, **6(b)** and **6(c)** compare snapshots of wave profiles at a time when the wave crest arrives at $x/d = 15$ for $\sigma =$
4 0.2, 0,4 and 0.6, respectively. For the smaller solitary wave, i.e. $\sigma = 0.2$, the figure shows good agreement of wave elevations
5 among the G3S, G9S and FNL method. However, the wave amplitude based on the G1S method fails to reach the target value
6 and the trailing waves are more visible than those in other methods. As the wave amplitude increases to 0.4, G3S and G9S
7 method's wave profiles (both the wave crest and trailing waves) are almost identical, but the trailing waves are still nearly
8 invisible for the FNL method's result. For a solitary wave of amplitude $\sigma = 0.6$, it is seen from **Figure. 6(c)** that the solitary
9 wave generated by the FNL method can not only reach the desired wave amplitude but also propagate with minor dispersive
10 trailing waves. But all the other three methods underestimate the maximum wave amplitude and they also introduce non-
11 negligible trailing waves. There also exist clear phase differences between Goring's method and the FNL method as can be
12 seen in **Figure. 6(c)**. Since the generated wave using the FNL method is higher than that of Goring's method, the
13 corresponding phase speed is also slightly larger. **Figure. 6(d)** shows temporal evolution of the maximum amplitude for the
14 three cases. G1S method's result of the maximum amplitude seems to first overpredict but then underpredict the wave height
15 during propagation. This is especially apparent for higher waves. This observation indicates that the dispersive effect in the
16 G1S method is much stronger when compared with the other three methods. One can also notice that, for $\sigma \geq 0.4$, the
17 maximum amplitude based on the G1S method seems to be much lower than the target value. A similar discrepancy was also
18 observed in Wu *et al.* [18] for $\sigma \geq 0.4$ by using the G1S method. Moreover, Wu *et al.* [18] and Hanssen *et al.* [41] have also
19 used the G9S method to generate solitary waves of amplitude $\sigma = 0.6$. As a comparison, the FNL method is proven to be able
20 to generate solitary waves much closer to desired ones, even for waves with amplitude as high as $\sigma = 0.6$.
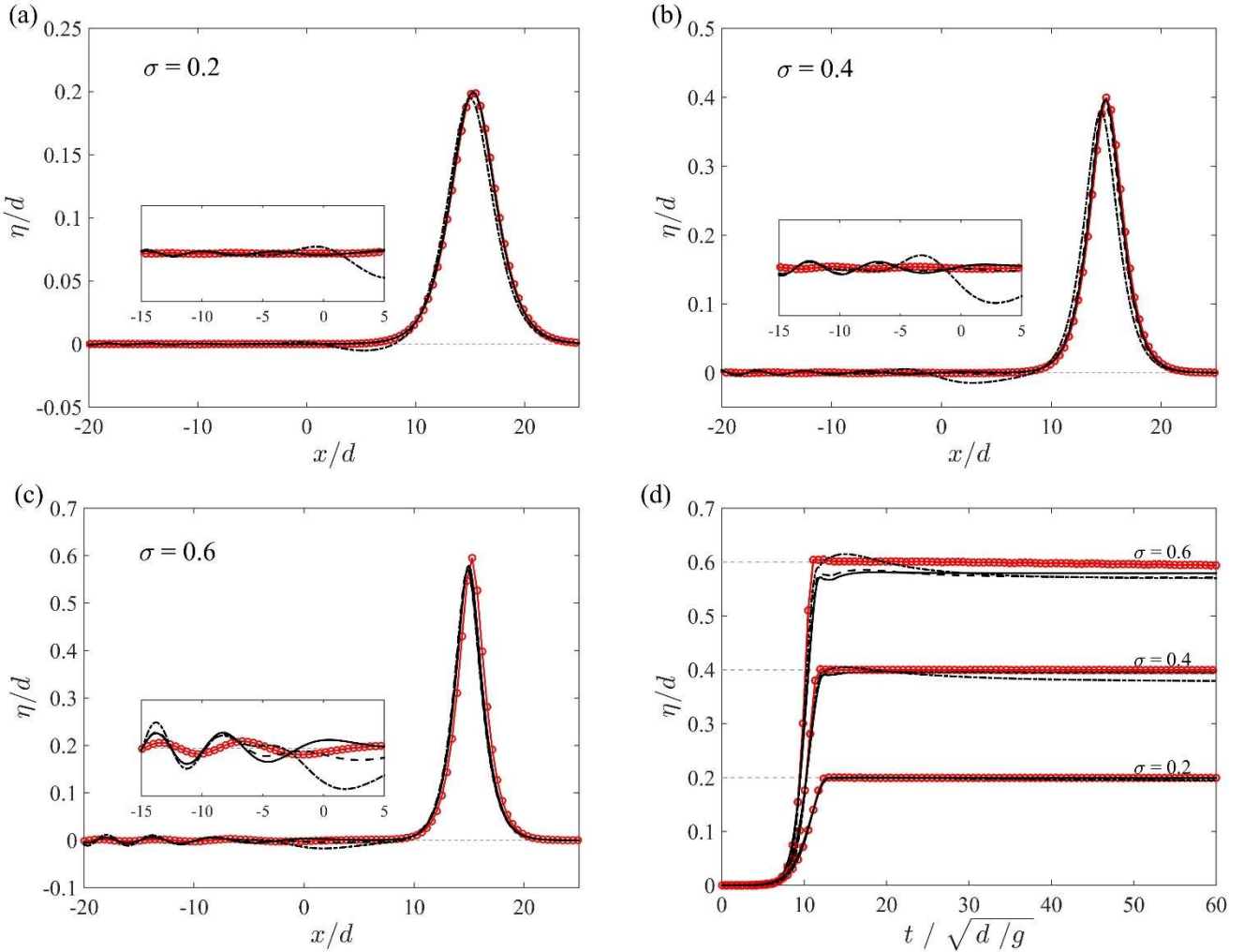
21

22

23 **Figure 6**. Subplots (a), (b) and (c) display snapshots of the wave profiles by using the G1S method ($\cdot - \cdot - \cdot$), the G3S method
24 ($- - -$), the G9S method (———) and the FNL method (—o—) for solitary wave of amplitude $\sigma = 0.2$, 0.4 and 0.6. Subplot
25 (d) shows temporal evolution of the maximum wave elevations for solitary wave of amplitude $\sigma = 0.2$, 0.4 and 0.6.

26   The cause of the deviation between Goring's method and the FNL method is mainly because horizontal velocities of

water particles are assumed uniform along the wave maker, while in the FNL method the fully nonlinear solution of horizontal velocity is directly imposed on the wave maker boundary. Therefore, the higher-order terms in solitary wave solutions become fairly important as σ increases. Goring's paddle-motion formula ignores the higher-order effects, which eventually results in some dispersion errors, causing both trailing waves and reduction in wave amplitude. In this way, the FNL method seems superior when it comes to higher-amplitude solitary waves. This also indicates the wave-generation mechanism rather than the numerical method resulting in disparity of numerical results when different wave-generation methods are used.

Based on the comparisons presented above, the use of a piston-type wave maker by the G9S method is accurate enough for solitary waves of amplitudes $\sigma \leq 0.4$, while the FNL method might be needed for much higher waves. In Sec.3.2, we will compare our numerical results with experimental measurements where the piston-type wave maker is used. The largest σ value considered therein is 0.4.

3.2 Head-on collision of solitary waves

3.2.1 Wave run-up at a wall

As for the reflection of solitary waves from a wall, He & Kashiwagi [49] investigated the interaction of a solitary wave with a vertical elastic plate. Ertekin *et al.* [50] in their study mentioned that the reflection process is equivalent to the head-on collision between two identical solitary waves, so that we can imagine that there is an exactly upright wall located at the collision center during the head-on collision. In this part, the G9S method is used for solitary wave generation. In present computations, a 2D domain with calm water depth *d* = 1m, tank height *H* = 3m and tank length *L* = 40m is assumed. The whole domain is evenly discretized into 600 elements in horizontal direction and 75 elements along the vertical direction. A time step is set as 0.02*s* in the time-domain simulations. A set of solitary waves with different normalized initial amplitudes, *A*/*d* = 0.1, 0.15, 0.2, 0.25, 0.3, 0.35, 0.4, 0.45, 0.5, 0.55, 0.6, are simulated. **Figure. 7** presents the comparison of the maximum run-up among Su & Mirie's [1] first-, second- and third-order approximation, Cooker *et al.*'s [26] numerical results, the experimental results of Camfield & Street [7] and Maxworthy [21]. According to Su & Mirie's [1] third-order solution, the non-dimensional maximum run-up can be quantified in the form as:

$$\sigma_{max} = 2\sigma + \frac{1}{2}\sigma^2 + \frac{3}{4}\sigma^3. \tag{12}$$
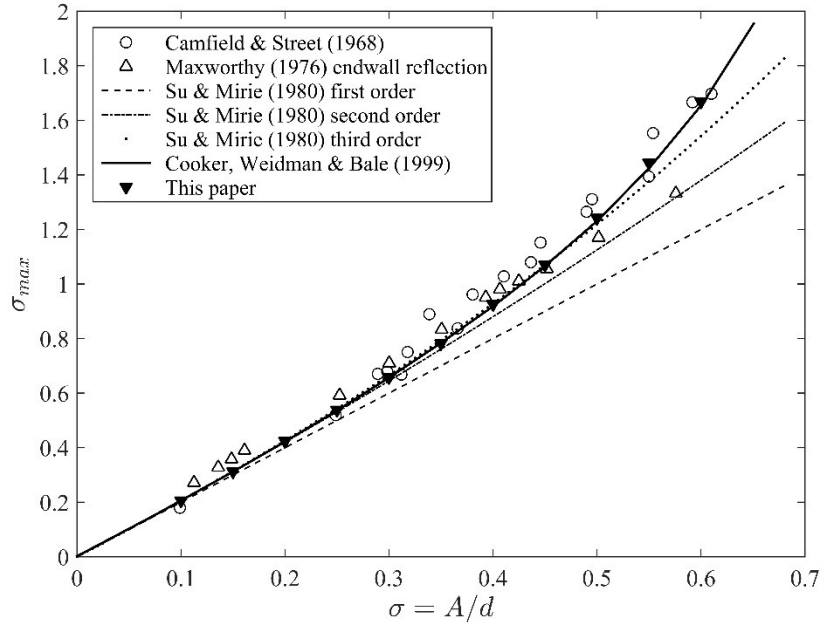

Figure 7. Maximum run-up versus incident wave amplitude.

From **Figure. 7**, it can be found that the results of the present HPC method are consistent with Su & Mirie's [1] third-order results except for higher incident waves. Both the results of our calculation and Cooker *et al.* [26] appear to be obviously higher than Su & Mirie's [1] third-order predictions when the incident wave amplitude is larger than 0.5, which indicates the importance of nonlinear terms higher than 3th order. The fourth-order or even higher order solutions might, therefore, be

required for predicting the maximum run-up in experiments. In our study, trailing waves are created due to the use of the G9S method. Consequently, the wave amplitude will be lower than the target value. To eliminate this effect, the wave maker signal has to be calibrated to generate the incident waves of desired amplitudes. In other words, the input wave should be slightly higher than the desired one during wave generation. The same technique is commonly implemented for generating high-amplitude solitary waves in physical wave flumes. One can see from **Figure. 7** that the present numerical results are in excellent agreement with Cooker *et al.*'s [26] results.

3.2.2 Comparison with experimental results

In this part, we validate our numerical model with experimental measurements of Chen & Yeh [2] on symmetric head-on collision of identical solitary waves with amplitudes $\sigma_R = \sigma_L = 0.4$. Here, $\sigma_R = A_R / d$ and $\sigma_L = A_L / d$ denote non-dimensional amplitude of the right- and left-running wave, respectively. **Figure. 8** shows wave crest trajectories of the present numerical results and experimental results with excellent agreement. Chen & Yeh [2] reported, in their study, that the phase speed of a solitary wave slowed down resulting from the reduction in amplitude after the collision. However, from the plot of crest trajectories and the slopes of the linear fitted lines in **Figure. 8**, it is clear that the wave speed of two solitary waves has slightly increased after the interaction, which is obviously contradictory with the conclusion of Chen & Yeh [2]. Similar to our report, Maxworthy [21] also mentioned, according to their experimental observation, that the reflected wave moved slightly faster than the incoming wave in spite of the attenuation in height. On the other hand, Byatt-Smith [20], Su & Mirie [1] and Chan & Street [24] concluded the unchanged wave amplitude after the head-on collision from either their theoretical predictions or numerical solutions. Fenton & Rienecker [23] also noticed the increase of wave speed for a returned solitary wave from a vertical wall. They suggested that even though the crest elevation was actually reduced, the trough of the first trailing wave might have played a significant role in increasing the 'effective wave height' (the vertical distance from the trailing trough to the main crest), which consequently results in the wave speed augment.
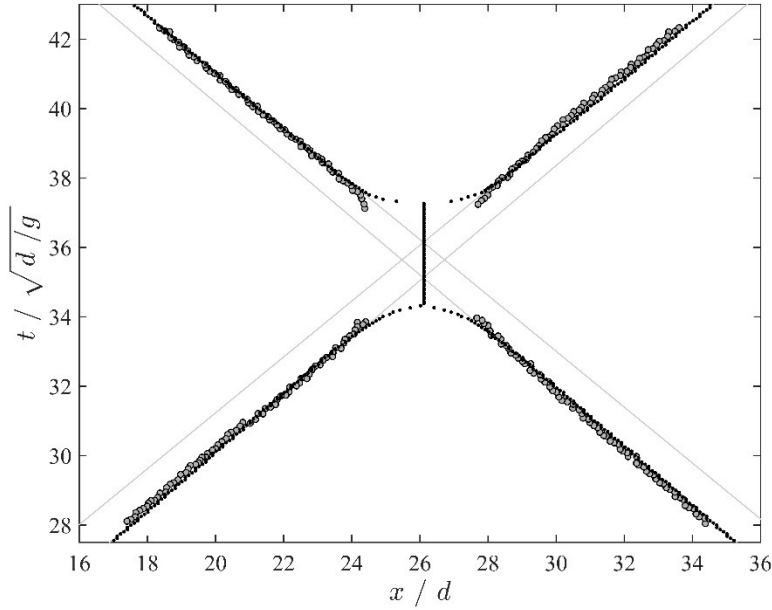
Figure 8. Wave-crest traces of the symmetric head-on collision of solitary waves with equal amplitude $\sigma_R = \sigma_L = 0.4$: ————— , linear fitting results of right- and left-running wave-crest trajectory before and after collision; ....., crest trajectories of our numerical results; ◦ , experimental measurements of Chen & Yeh [2].
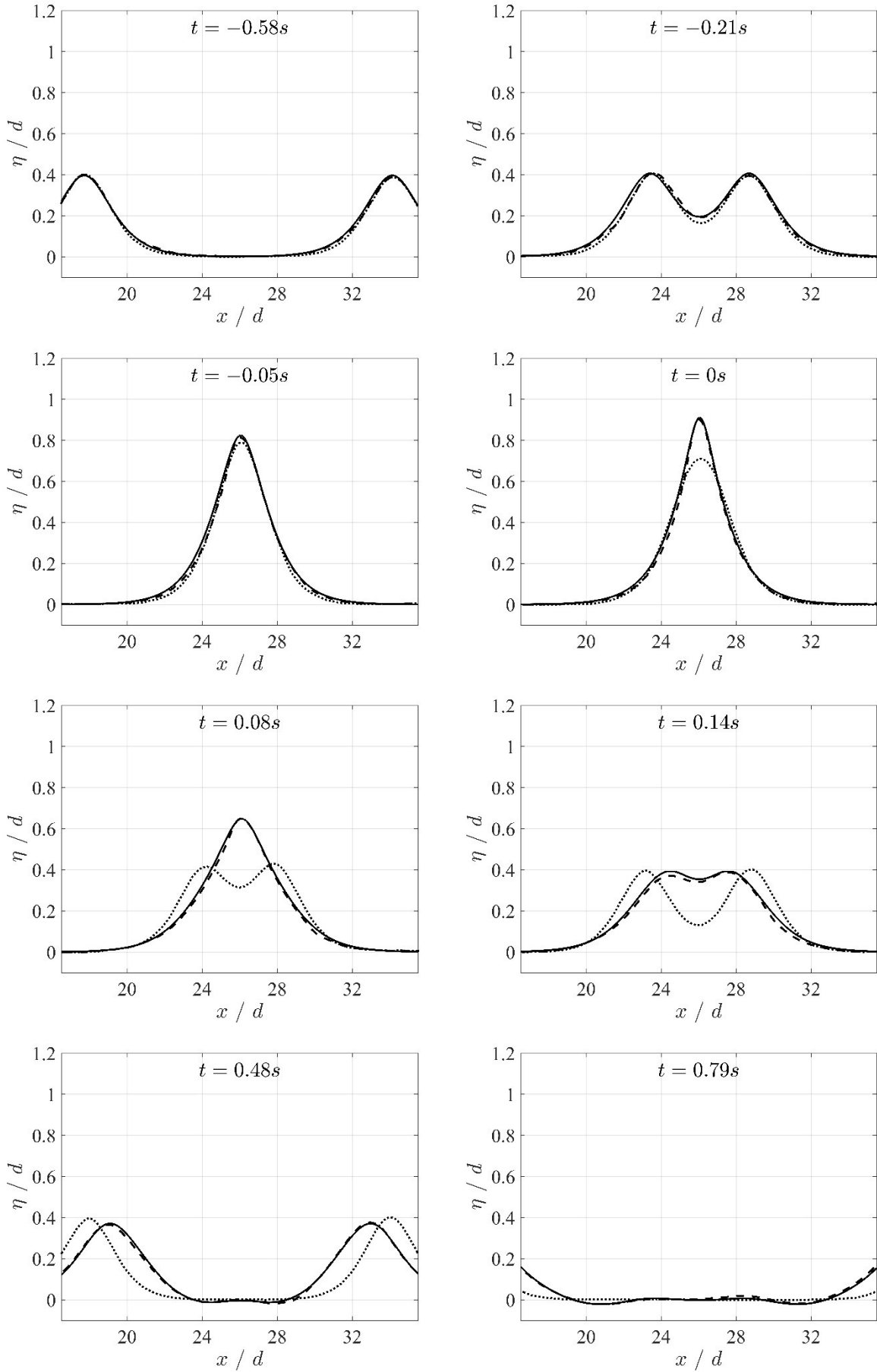
Figure 9. The comparison of free surface profiles during the head-on collision of identical solitary waves with amplitude $\sigma_R = \sigma_L = 0.4$: ———, numerical results based on the HPC method; - - - - -, experimental results from Chen & Yeh [2]; ⋯⋯, linear superposition of the counter-propagating KdV solitons.

Figure. 9 presents the comparison of the numerical, experimental and linear KdV solutions of the free-surface profiles for the head-on collision of solitary waves with amplitudes $\sigma_R = \sigma_L = 0.4$. The moment when the maximum run-up occurs corresponds to $t = 0$s in the experiment of Chen & Yeh [2]. Satisfactory agreement of our numerical results and the experimental results can be seen in **Figure. 9**, yet the linear KdV solution fails to predict the collision process. On the other hand, we also notice that the wave profile from the experiment slightly differs from our numerical result especially for the trailing waves at $t = 0.79$s. In fact, the right- and left-running solitary wave in the experiment were marginally different in amplitude. The right-running wave was a little higher than the left-running wave after the collision in the experiment, which consequently results in the first trailing wave crest behind the right-running wave faintly higher. Conversely, the two waves are the same in amplitude in our numerical study, so that the trailing waves are, correspondingly, symmetric at $t = 0.79$s. As mentioned in Chen & Yeh [2], the phase lag between the linear KdV solution and experimental measurements was caused by the additional run-up process.

The trailing waves we mentioned above are also manifested in **Figure. 10**. Due to the asymmetry of solitary waves in the experiment, the phase speed of the right-running wave is slightly larger than that of the left-running wave, which leads to minor augment in celerity of the first trailing wave behind the right-running wave. Thus, it can be found, from **Figure. 10**, that the numerical and experimental trailing wavetrain profiles are in reasonable agreement for the left-running wave, but not for the right-running wave. The first trailing wave trough in the experiment propagates slightly faster than that in the numerical calculation. Considering that the trailing waves are minor in amplitude, the trailing waves of the present numerical result agree fairly well with the third-order prediction of Su & Mirie [1]. The validation strongly indicates the capability of our numerical model based on the HPC method in successfully simulating head-on collision of solitary waves.
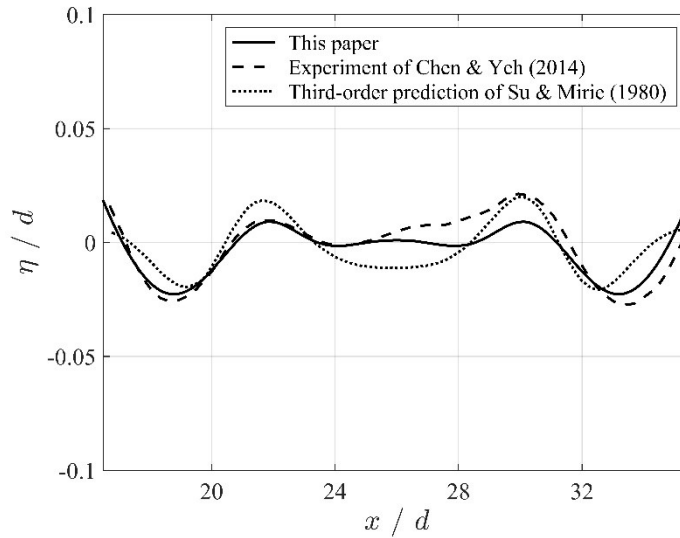

Figure 10. Comparison of dispersive trailing waves of the present work with experimental result of Chen & Yeh [2] and the third-order prediction of Su & Mirie [1] at $t = 0.96$s for solitary waves of amplitudes $\sigma_R = \sigma_L = 0.4$.

4. Analysis of wave-wave interaction

4.1 Symmetric and asymmetric head-on collision

In this part, we present numerical results of head-on collision cases. Four simulation scenarios are considered, which are listed in **Table. 3**. The time step here is $\Delta t = 0.02$s.

Table 3. List of numerical simulation scenarios.

|	Case	Water depth d (m)	Tank length L (m)	Right-running wave σ_R	Left-running wave σ_L	Collision center x/d
Symmetric collision	1			0.2	0.2	- 40.89
	2	1	300	0.4	0.4	- 24.16
Asymmetric collision	3			0.2	0.4	- 31.16
	4			0.3	0.4	- 37.56

12

1 **(a) Symmetric collision**

2   **Figure. 11** shows the spatial-temporal profiles of solitary waves propagating in opposite directions for Case2. As for the

3 phase shifts, Craig *et al.* [3] proposed that the crest trajectories can be asymptotically expressed as $x = c_i t + a_i$ $(i = 1, 2)$ prior

4 to collision and $x = c_i^+ t + a_i^+$ $(i = 1, 2)$ after collision, in which $i = 1$, 2 represent right- and left-running waves, respectively.

5 Since the phase shift varies with measurement points [23], Craig *et al.* [3] suggested that the phase shift $\Delta\theta$ can be calculated

6 at the time $t = \tau$ to reduce this variance:

7 $$\Delta\theta = \left(a_i^+ - a_i\right) + \tau\left(c_i^+ - c_i\right), (i = 1, 2). \qquad (13)$$

8 Here τ is the moment when the maximum run-up occurs during the collision. **Figure. 12** gives crest traces of solitary waves

9 for this symmetric head-on collision. We present the asymptotic functions for these trajectories in the plot, just as the same

10 way as Craig *et al.* [3] proposed. From the asymptotic functions, we can also find that wave speeds increased after their

11 collision. In this simulation, $\tau / \sqrt{d / g}$ = 426.34. The phase shifts for right- and left-running wave are calculated by **Eq. 13**

12 as $\Delta\theta_R / d = 0.9459$ and $\Delta\theta_L / d = 0.9486$, respectively. We have to remark that these phase shifts are absolute values

13 representing a retardation of waves after the collision. According to Su & Mirie's [1] third-order prediction, the uniform phase

14 shift for the right- and left-running wave is expressed respectively as:

15
$$\left.\begin{aligned}
\frac{\Delta\theta_R}{d} &= \left(\frac{\sigma_L}{3}\right)^{\frac{1}{2}}\left(1 + \frac{1}{8}\sigma_L + \frac{3}{4}\sigma_R\right) \\
\frac{\Delta\theta_L}{d} &= -\left(\frac{\sigma_R}{3}\right)^{\frac{1}{2}}\left(1 + \frac{1}{8}\sigma_R + \frac{3}{4}\sigma_L\right)
\end{aligned}\right\}. \qquad (14)$$

16 However, the phase shifts predicted by **Eq. 14** in this case yield $\Delta\theta_R / d = \Delta\theta_L / d = 0.49$, which is much lower than the

17 results of our numerical calculation. On the other hand, the experimental measurements of the phase shifts in Chen & Yeh [2]

18 give 0.98 for the right-running wave and 1.1 for the left-running wave, which are in reasonable agreement with our present

19 numerical results. The difference between our calculations and Su & Mirie's [1] third-order approximation will be further

20 discussed in details in Sec. 4.2.

21
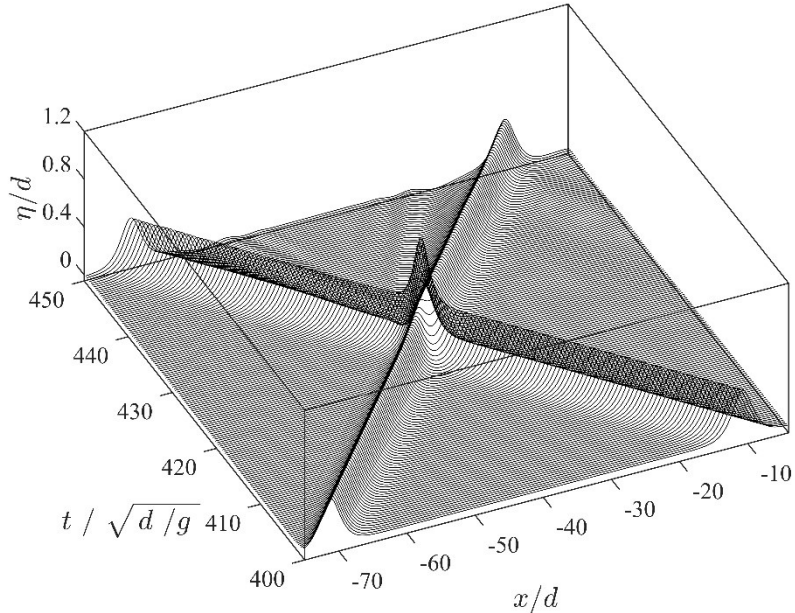
22 **Figure 11**. The surface profiles of head-on collision of solitary waves with an equal wave amplitude $\sigma = A/d = 0.4$.
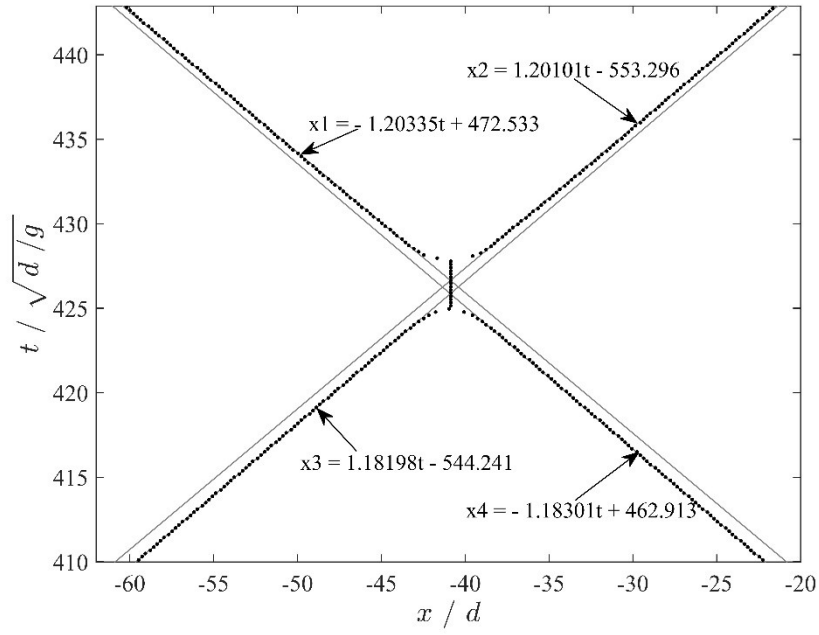
Figure 12. Wave-crest traces of symmetric head-on collision for solitary waves with an equal amplitude $\sigma = A/d = 0.4$: ——————, linear fitting lines of the right- and left-running wave-crest trajectories before and after the collision; $\cdots\cdots$, crest trajectories of the present numerical calculations.
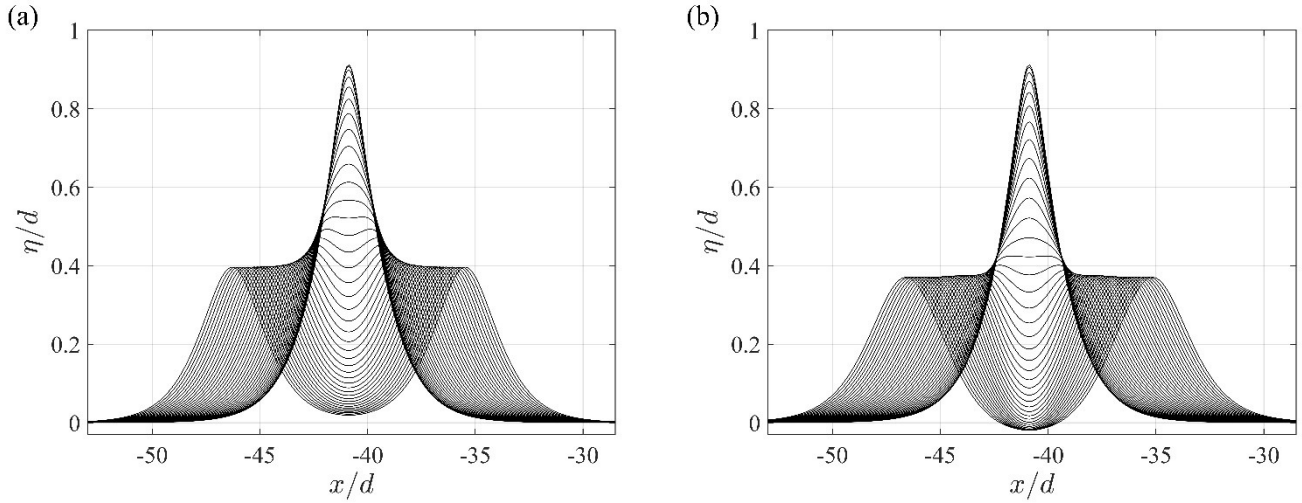

Figure 13. Plots of the free-surface profiles at different time for waves with amplitudes $\sigma_R = \sigma_L = 0.4$: (a) before collision for $-10 < t/\sqrt{d/g} < 0$ and (b) after collision for $0 < t/\sqrt{d/g} < 10$.

Figure. 13(a) and **Figure. 13(b)** present the collision run-up and run-down process, respectively. We define the time when maximum run-up occurs as $t = 0$s, so the time before the collision is negative ($t < 0$) and the time after the collision is positive ($t > 0$). From **Figure. 13**, we can clearly find that the maximum run-up during the collision is larger than the sum of two incident amplitudes. The results of the maximum run-up can be found in **Table 4**. Moreover, the run-up and run-down process of the head-on collision are not symmetric. In the collision run-up process, the free surface elevation at the collision center gradually rises up with an inflection point of the wave profile at $\eta/d \approx 0.55$, while the inflection point occurs at $\eta/d \approx 0.43$ in the run-down process. In **Figure. 13(b)**, it shows that the amplitude of each wave is slightly attenuated after re-emerging. Furthermore, the wave profile at the collision center is also lower than the quiescent water level between two departing waves.

(b) Asymmetric collision

14

For asymmetric head-on collision, we choose to first generate the higher wave, which travels downstream to be reflected from the tank wall and then collides with the lower wave. In laboratory experiments, the wave amplitude would attenuate during propagation due to water viscosity and dispersion by reflection from the wall. In our study, despite the absence of water viscosity in potential flow, there is still a dispersion factor causing reduction in the wave amplitude. To produce a reflected solitary wave with a desired amplitude, we need to calibrate the input wave amplitude. Take asymmetric collision Case3 in **Table 2** for example, the maximum run-up happens at $\tau / \sqrt{d / g}$ = 420.39. **Figure. 14** displays the collision process between two solitary waves of amplitudes $\sigma_R = 0.2$ and $\sigma_L = 0.4$. **Figure. 15** shows the positions of wave crests prior to and after the collision. The third-order approximation of maximum wave run-up for asymmetric head-on collision by Su & Mirie [1] is

$$\sigma_{\max} = \sigma_R + \sigma_L + \frac{\sigma_R \sigma_L}{2} + \frac{3}{8} \sigma_R \sigma_L (\sigma_R + \sigma_L). \qquad (15)$$

In this asymmetric collision, the maximum run-up of the present numerical analysis and the third-order prediction by **Eq.15** are very close to each other, which are summarized in **Table 4**. In **Figure. 16**, the smaller wave is gradually swallowed by the larger one until only one wave crest is formed in the run-up process. Unlike the symmetric collision, the single crest moves with a changing speed instead of standing at a fixed point, which can also be seen in **Figure. 15** in the collision area (marked as +). In the run-down process, both the two waves do not re-gain their initial amplitudes and the smaller wave reemerges from the single crest.

Table 4. Non-dimensional results of symmetric and asymmetric head-on collision.

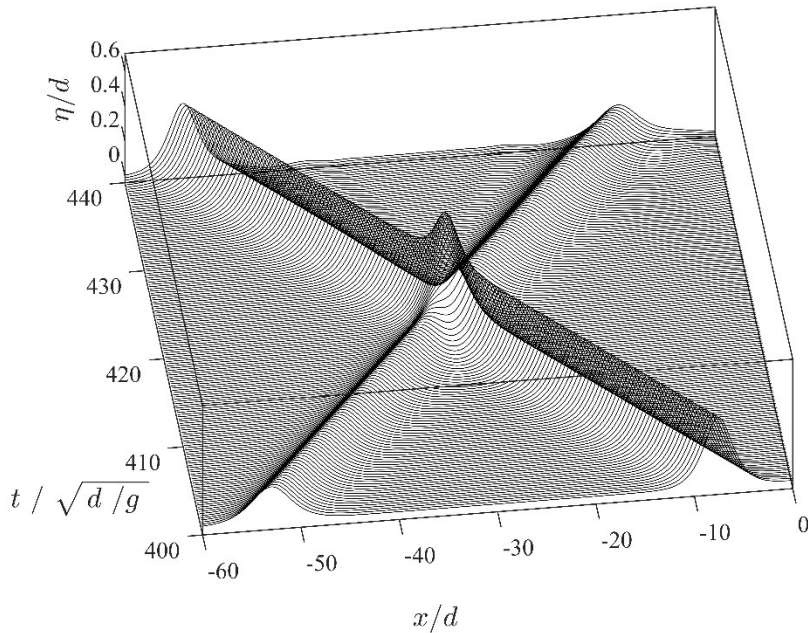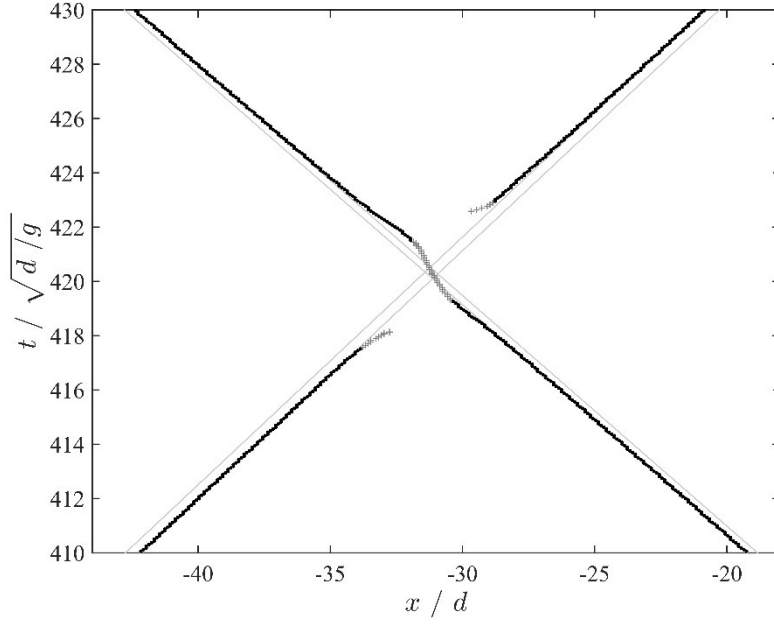|	Symmetric collision				Asymmetric collision			
	Case1		Case2		Case3		Case4	
	$\sigma_R = \sigma_L = 0.2$		$\sigma_R = \sigma_L = 0.4$		$\sigma_R = 0.2$	$\sigma_L = 0.4$	$\sigma_R = 0.3$	$\sigma_L = 0.4$
Third-order approximation of the maximum run-up	0.4260		0.9280		0.6580		0.7915	
Numerical maximum run-up	0.4243		0.9118		0.6486		0.7815	
Amplitude after collision	0.1889	0.1886	0.3786	0.3790	0.1939	0.3857	0.2847	0.3841
Reduction ratio of amplitude	5.56%	5.70%	5.35%	5.25%	3.05%	3.57%	1.53%	5.30%

Figure 14. The surface profiles of the head-on collision of solitary waves with wave amplitudes $\sigma_R = 0.2$ and $\sigma_L = 0.4$.

1
2 **Figure 15**. Wave-crest traces of the asymmetric head-on collision for solitary waves with wave amplitudes $\sigma_R = 0.2$ and
3 $\sigma_L = 0.4$ ： ——— ， linear-fitting lines of right- and left-running wave-crest trajectories prior to and after the collision；
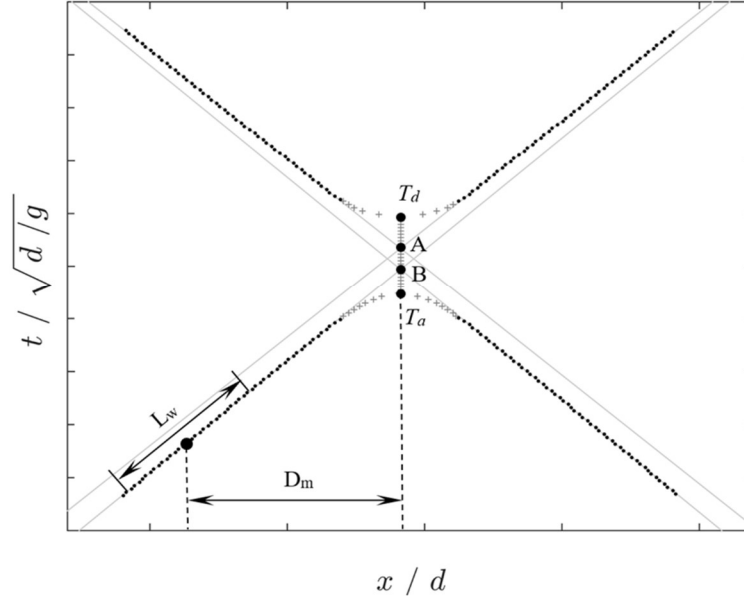4 • and ＋， crest trajectories of the present numerical results.
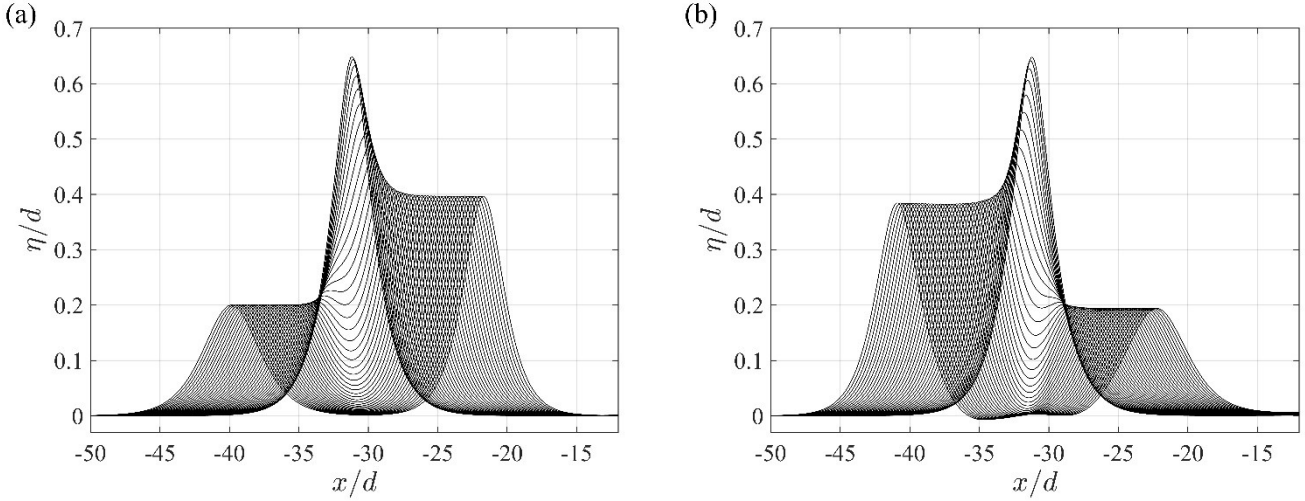
5
6 **Figure 16**. Plots of the temporal variation of the free surface profile for wave amplitudes $\sigma_R = 0.2$ and $\sigma_L = 0.4$ ： (a) before
7 the collision for $-8.3 < t / \sqrt{d / g} < 0$; (b) after the collision for $0 < t / \sqrt{d / g} < 8.3$.

4.2 Investigation of phase shifts for the head-on collision

9   As mentioned in Sec. 4.1, Chen & Yeh's [2] experimental results of the phase shifts do not agree with the third-order
10 prediction by Su & Mirie [1]. This discrepancy was also noticed by Craig *et al.* [3] in their fully nonlinear numerical study.
11 In this part, we will account for the reason why the prediction by **Eq. 14** underestimates the phase shifts.
12   For the symmetric collision, the free surface profile at the collision center is gradually elevated as the two solitary waves
13 approach each other in the run-up process. At the same time, the amplitude of each wave grows until the wave amplitude is
14 equal to the free surface elevation at the collision center. The process corresponds to the appearance of the inflection of the
15 wave profile in **Figure. 13**. During this process, there is a moment when the wave speed is close to infinity until a single crest
16 appears at the collision center. This observation can be referred to the theoretical analysis of Cooker *et al.* [26]. It can be
17 found from **Figure. 17** that some crest trajectories (symbols '+') close to the collision center deviate from the fitting lines due
18 to the dramatic growth of wave speed in a short period. The inclusion of these crest trajectories close to the collision center
19 to get the linear fitting lines will affect the calculations of the phase shifts by **Eq. 13**. In this case, these trajectories close to
20 the collision center are reasonably discarded while obtaining the linear fitting lines by a least-squared method. In the following
21 texts, for simplicity we will use 'deviated data' and 'fitting data' to stand for the crest trajectory data close to the collision

1 center and remnant fitting data, respectively.

2

3 **Figure 17**. Wave-crest traces of symmetric head-on collision：⸻，linear fitting lines of crest trajectories；• and
4 ＋，the present numerical results.

5

6 To calculate the phase shifts by **Eq. 13**, the main task is to specify the linear fitting functions based on the 'fitting data'
7 prior to and after the head-on collision. We find that the fitting function varies with both the distance D_m from mearsurement
8 point to the collision center and the length of data window L_w, which are demonstrated in **Figure. 17**. The measurement point
9 is fixed at the center of each data window. The following model of window length L_w is conducted in specifying the linear
10 fitting functions:

11
$$L_w = \begin{cases} [5,10], & \text{if } D_m \in [1,10] \\ (10,20], & \text{if } D_m \in (10,20] \\ (20,40], & \text{if } D_m \in (20,40] \\ (40,60], & \text{if } D_m \in (40,+\infty] \end{cases}. \tag{16}$$

12 The slope of wave-crest trace changes dramatically close to the collision center. Therefore, the data window should be
13 shorter. However, considering there still exist numerical errors when recording the crest trajectories, the window length should
14 not be set too small to avoid distortion of the fitting lines. For the measurement point closer to the collision center, the
15 calculation of the phase shifts shows that **Eq. 16** can perform well in getting fitting lines based on 'fitting data'.
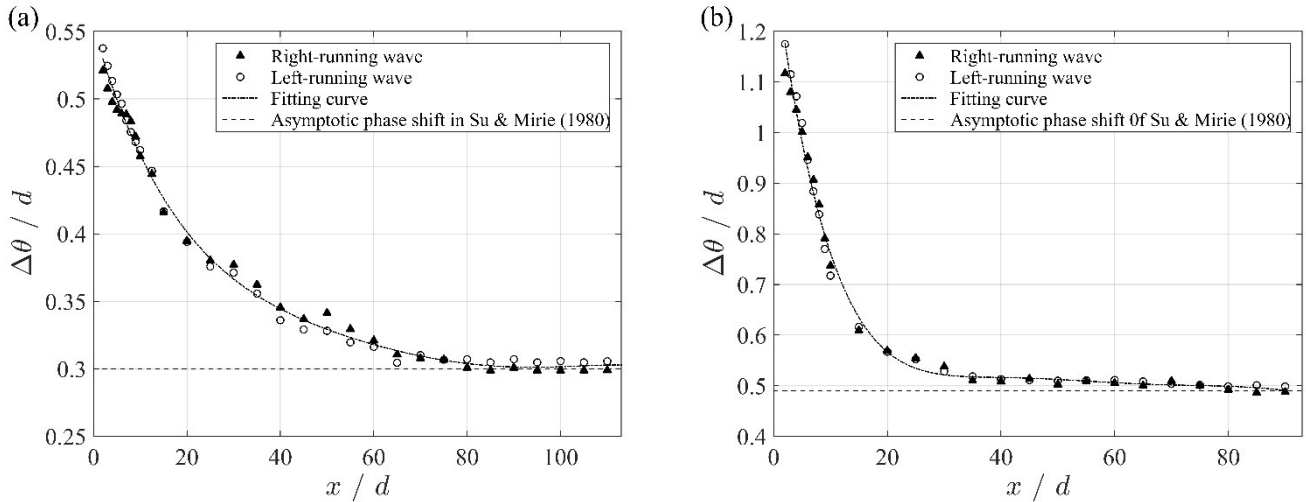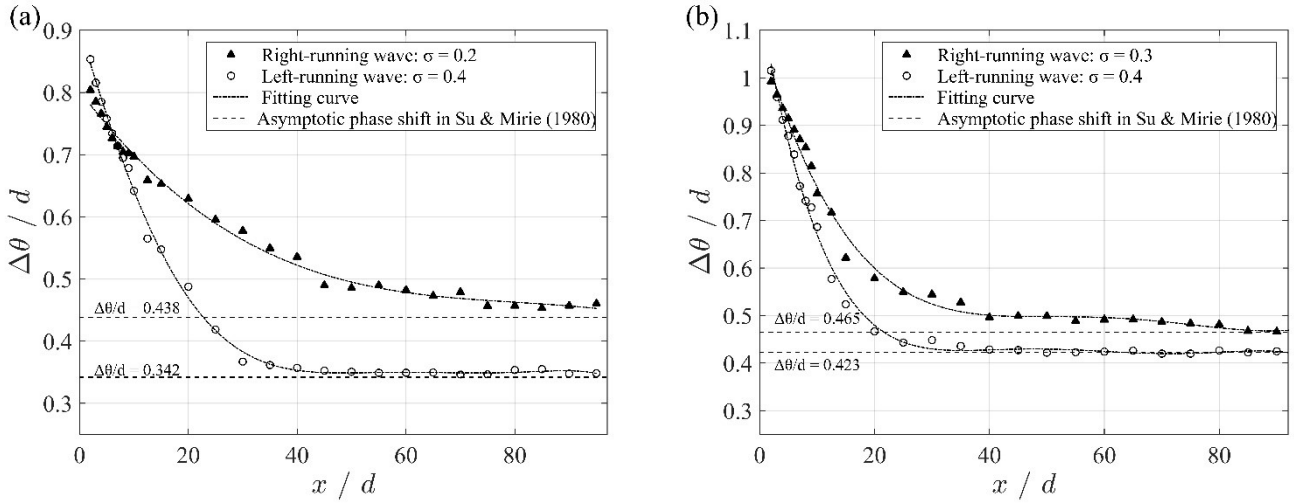

16

17 **Figure 18**. Phase shifts versus the measurement distance from the collision center for symmetric head-on collision of solitary
18 waves: (a) $\sigma_R = \sigma_L = 0.2$ and (b) $\sigma_R = \sigma_L = 0.4$. The asymptotic value for $\sigma_R = \sigma_L = 0.2$ and $\sigma_R = \sigma_L = 0.4$ is $\Delta\theta/d = 0.3$
19 and $\Delta\theta/d = 0.49$, respectively.

Fenton & Rienecker [23] pointed out that the measurement of phase shifts is sensitive to the distance from the collision center. They found that their numerical results of the phase shifts near to the collision center are in consistent with Su & Mirie's [1] another third-order phase shift limit, namely

$$\left.\begin{array}{l}\dfrac{\Delta\theta_R}{d}=\left(\dfrac{\sigma_L}{3}\right)^{\frac{1}{2}}\left(1+\dfrac{1}{8}\sigma_L+\dfrac{23}{4}\sigma_R\right)\\[4mm]\dfrac{\Delta\theta_L}{d}=-\left(\dfrac{\sigma_R}{3}\right)^{\frac{1}{2}}\left(1+\dfrac{1}{8}\sigma_R+\dfrac{23}{4}\sigma_L\right)\end{array}\right\},\qquad(17)$$

which is called immediate phase shift. The immediate phase shift by **Eq. 17** for $\sigma_R=\sigma_L=0.2$ and $\sigma_R=\sigma_L=0.4$ is $\Delta\theta/d=0.56$ and $\Delta\theta/d=1.22$, respctively. Excellent agreement can be observed from **Figure. 18**, between our numerical results near to the collision center and the prediction by **Eq. 17**.

For $\sigma_R=\sigma_L=0.4$, Chen & Yeh [2] dealt with their experimental data, actually, using the same window model as we proposed in **Eq. 16** and obtained $\Delta\theta_R/d=0.98$ and $\Delta\theta_L/d=1.1$. The 'deviated data' were also discarded in their analysis. We can translate their 'fitting data' into our window model: $D_m\approx5$ and $L_w\approx6.5$. Our calculation yields $\Delta\theta_R/d=1.0$ and $\Delta\theta_L/d=1.01$, which are in good agreement with the experimental results. On top of this, another satisfactory discovery is that the calculated phase shifts are asymptotic to the prediction by **Eq. 14** if the measurement point is far away from the collision center. The approximation of the phase shifts by **Eq. 14** is named as the uniform phase shift when two departing waves are far enough away from each other. Chen & Yeh [2] thought their calculation of the phase shift based on the 'fitting data' is larger than the asymptotic value of **Eq. 14** mainly resulting from the solitary wave tilting backward with respect to the direction of its propagation after the collision. In fact, the 'fitting data' used by Chen & Yeh [2] are very close to the collision center. The result they calculated corresponds, actually, to the immediate phase shift, but they compared their immediate phase shift with the asymptotic value of the uniform phase shift by **Eq. 14**. This is the main reason why they mistakenly concluded that the third-order prediction (**Eq. 14**) of Su & Mirie [1] could not predict their experimental measurements of the phase shift.

Figure 19. Phase shifts versus the measurement distance from the collision center for asymmetric head-on collision of solitary waves: (a) $\sigma_R=0.2$, $\sigma_L=0.4$ and (b) $\sigma_R=0.3$, $\sigma_L=0.4$.

Figure. 19 provides phase shifts versus the measurement distance from the collision center for asymmetric head-on collision. Both the immediate phase shifts and the uniform phase shifts of our calculations are in good agreement with the third-order asymptotic results. We can notice that the retardation of the smaller solitary wave is more severe than the higher wave considering the uniform phase shift, which can also be seen from **Figure. 15**.

As we have mentioned above, the measurement of the phase shifts strongly depends on the distance from the collision center because of the change of wave speed after the collision. Fenton & Rienecker [23] found that even though the spatial phase shift changes with measurent positions, the phase lag in time ΔT remains unchanged at the collision center, which is equivalent to the length of $\overline{AB}$ segment in **Figure. 17** for symmetric head-on collision. However, it is still difficult to evaluate ΔT in practice because the location of point A and B in **Figure. 17** depends on the linear fitting lines. As we have discussed,

the determination of the fitting functions is associated with D_m and L_w. Under this circumstance, Cooker et al. [26] proposed to use the wall residence time $T_r = T_d - T_a$, alternatively, as the definition of phase lag in time. T_a is the attachment time at which the incoming wave arrives at the vertical wall and T_d is the detachment time at which the reflected wave leaves the wall. The equivalent attachment and detachment time for symmetric head-on collision are defined in **Figure. 17**. The wall residence time given by Cooker et al. [26] is

$$\frac{T_r}{\sqrt{d/g}} = \frac{4\kappa_0}{\sqrt{3}}\left(\sigma^{-1/2} + \frac{1}{8}\sigma^{1/2}\right) ,\qquad (18)$$

where $\kappa_0 = \tanh^{-1}(1/\sqrt{3})$.

  Figure. 20 records the maximum amplitude versus time for symmetric head-on collision. **Figure. 20(a)** shows the comparison of the present results with the numerical results of Cooker et al. [26] for $\sigma_R = \sigma_L = 0.2$ with excellent agreement. **Figure. 20(b)** gives the present numerical result, experimental result of Chen & Yeh [2] and numerical result of Craig et al. [3] for $\sigma_R = \sigma_L = 0.4$. Our numerical result of maximum wave amplitudes agrees well with Cooker et al.'s [26] numerical result, while the experimental result of the maximum run-up is smaller than our numerical result. The wall residence time of our numerical results and the solutions by **Eq.18** for different cases are summarized in **Table 5**. For asymmetric collision, **Eq.18** is not applicable.

Table 5. The wall residence time for symmetric collisions and fully interacting time for asymmetric collisions.

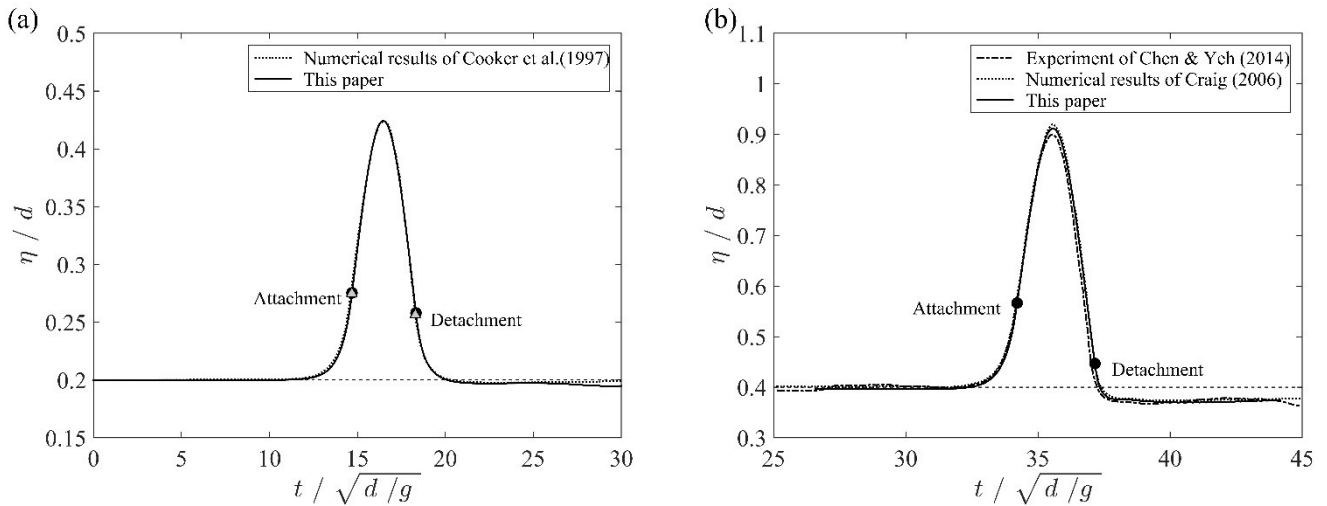| Wall residence time or fully interacting time	Type of collision	Case	Present numerical result	Theoretical result (**Eq.18**)
$\dfrac{T_r}{\sqrt{d/g}}$	Symmetric collision	$\sigma_R = \sigma_L = 0.2$	3.633	3.672
		$\sigma_R = \sigma_L = 0.4$	2.944	2.970
$\dfrac{T_f}{\sqrt{d/g}}$	Asymmetric collision	$\sigma_R = 0.2 \mid \sigma_L = 0.4$	4.323	NA
		$\sigma_R = 0.3 \mid \sigma_L = 0.4$	3.630	NA

Figure 20. Temporal variation of the maximum amplitude for symmetric head-on collision. (a) The comparison of the our numerical results with the numerical results of Cooker et al. [26], here $\sigma_R = \sigma_L = 0.2$. (b) The comparison of the our results with the numerical results of Craig et al. [3] and the experimental measurements of Chen & Yeh [2], here $\sigma_R = \sigma_L = 0.4$. Attachment and detachment points are indicated: Δ from Cooker et al. [26] and $\bullet$ from the present study.
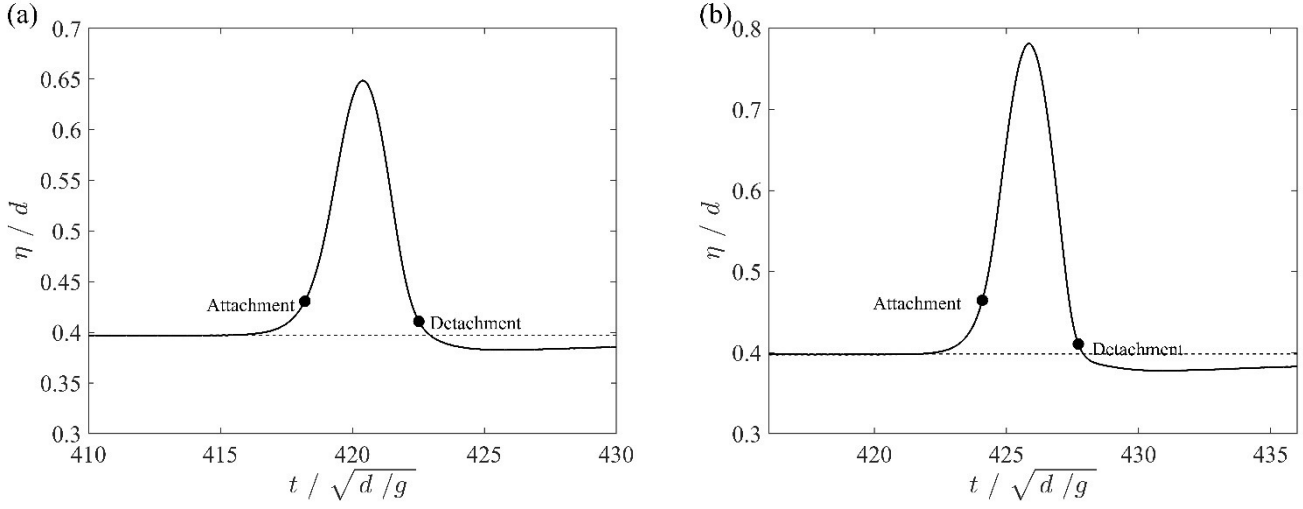
Figure 21. Temporal variation of the maximum amplitude for asymmetric head-on collision. (a) $\sigma_R = 0.2$, $\sigma_L = 0.4$. (b) $\sigma_R = 0.3$, $\sigma_L = 0.4$. Attachment and detachment point are indicated.

Figure. 21 shows the maximum amplitude versus time of the higher solitary wave for both the two asymmetric head-on collision cases, i.e. $\sigma_L = 0.4$. During the collision, we can always record the crest trajectory of the higher wave because the higher wave gains height without losing its crest by swallowing the smaller one. On the other hand, there is a dramatic leap of the crest elevation for the smaller solitary wave when it is swallowed, shown in **Figure. 16**.

Although the attachment and detachment point are proposed in the study on the reflection of a solitary wave from a vertical wall, we can still identify them in asymmetric head-on collision. In fact, the attachment and detachment point in symmetric or asymmetric head-on collision are the critical time to divide the whole collision process into two parts. There are two crests before the attachment and after the detachment, while there is only a single crest between the attachment and detachment time. So we can define the 'wall residence time' in wall reflection of a solitary wave as general fully interacting time T_f, namely

$$T_f = T_d - T_a \ , \tag{19}$$

which can be applied in both symmetric and asymmetric head-on collision. The numerical results of two asymmetric collision cases are summarized in **Table 5**. No researchers have investigated the analytical expressions of the attachment and detachment time for the asymmetric collision according to authors' knowledge, which requires further research in the future.

4.3 Overtaking collision

Overtaking collision of two solitary waves is considered as a 'strong' wave-wave interaction, which means that it takes a long duration for a larger solitary wave to catch up with, interact with, overtake and separate from the smaller one. There is a slight modification of wave amplitude and velocity after the collision, which has been discussed by Craig *et al.* [3] and Li [51]. The higher solitary wave experiences a positive phase shift while the smaller wave is retarded after the interaction.

In order to determine the numerical phase shifts of solitary waves after the overtaking collision, we take two locations X_1 and X_2 ($X_2 \geq X_1$). When passing these locations, the two solitary waves are clearly separated. The collision domain is between these two locations. The phase shifts can be evaluated according to Li [51] as

$$\hat{s}_i = L_0 - c_i \Delta t_i, (i=1,2), \tag{20}$$

where $L_0 = X_2 - X_1$ and c_i (i=1,2) is the ninth-order phase speed according to Fenton [19]. Δt_i (i =1, 2) is the time interval of a wave crest passing these two locations.

Li [51] gave the theoretical phase shifts for the two solitary waves in the form of

$$\left. \begin{aligned} s_1 &= \frac{1}{\tilde{\mu}_1} \ln \frac{(\tilde{\mu}_2 - \tilde{\mu}_1)^2}{(\tilde{\mu}_2 + \tilde{\mu}_1)^2} \\ s_2 &= \frac{1}{\tilde{\mu}_2} \ln \frac{(\tilde{\mu}_2 - \tilde{\mu}_1)^2}{(\tilde{\mu}_2 + \tilde{\mu}_1)^2} \end{aligned} \right\}, \tag{21}$$

20

where $\tilde{\mu}_1 = \sqrt{3\sigma_1}$, $\tilde{\mu}_2 = -\sqrt{3\sigma_2}$, $\sigma_1 = A_1/d$ and $\sigma_2 = A_2/d$ are dimensionless wave amplitude of the higher solitory wave and the smaller one, respectively. d is the calm water depth. Since $s_1 > 0$ and $s_2 < 0$, the higher wave is shifted forward and the smaller wave shifts backward after the interaction.

Lax [28] has categorized the overtaking collision of two solitary waves based on the ratio between the two initial amplitudes σ_1/σ_2 ($\sigma_1 > \sigma_2$): (a) $1 < \dfrac{\sigma_1}{\sigma_2} < \dfrac{3+\sqrt{5}}{2}$, (b) $\dfrac{3+\sqrt{5}}{2} < \dfrac{\sigma_1}{\sigma_2} < 3$, (c) $\dfrac{\sigma_1}{\sigma_2} > 3$. However, Craig *et al.* [3] found that the category given by Lax [28] seemed unable to accurately predict larger amplitude ratio cases, and proposed a revised criterion based on their experimental and numerical results, namely

$$1 < \frac{\sigma_1}{\sigma_2} \le 2.941 \quad , \text{category (a);}$$

$$2.941 < \frac{\sigma_1}{\sigma_2} \le 3.536 \quad , \text{category (b);}$$

$$\frac{\sigma_1}{\sigma_2} > 3.536 \quad , \text{category (c).}$$

In the present study, selected overtaking collision cases will be simulated and the results will be validated with the exsiting numerical and experimental results. The present numerical results will also be used to check the applicability of the categories proposed in Lax [28] and Craig *et al.* [3].
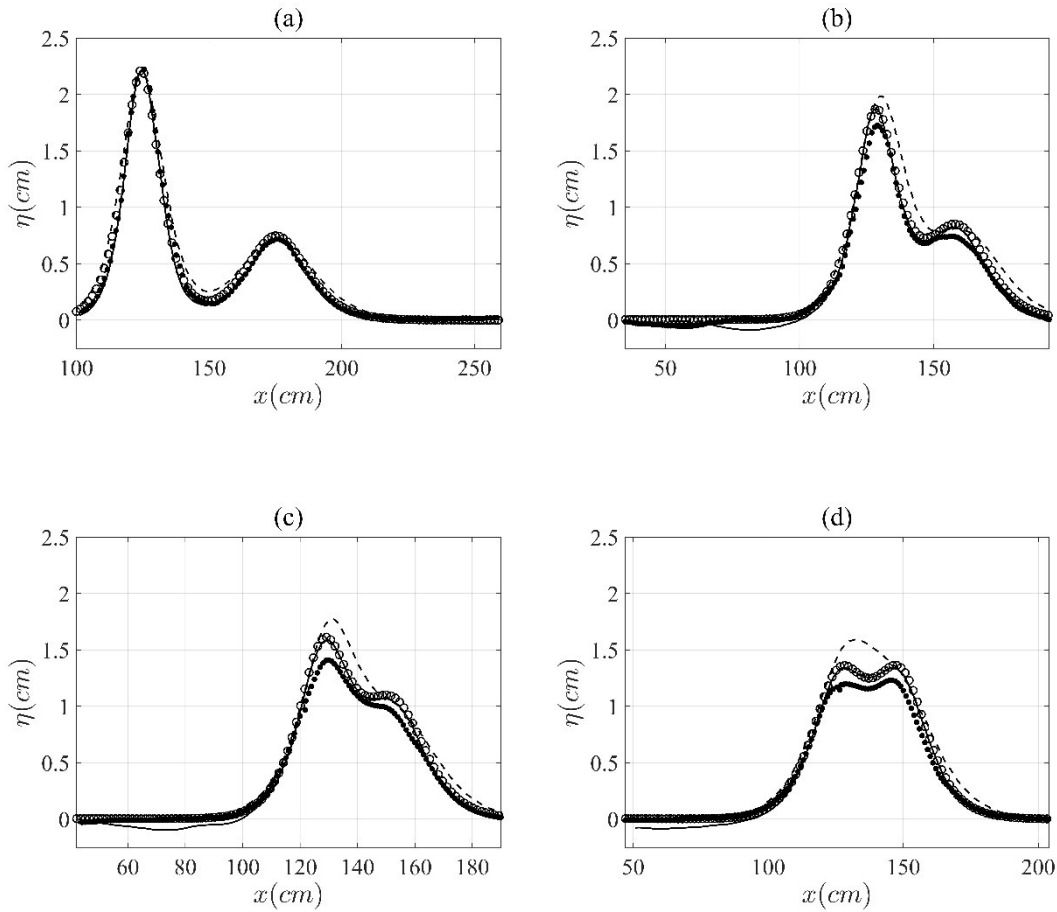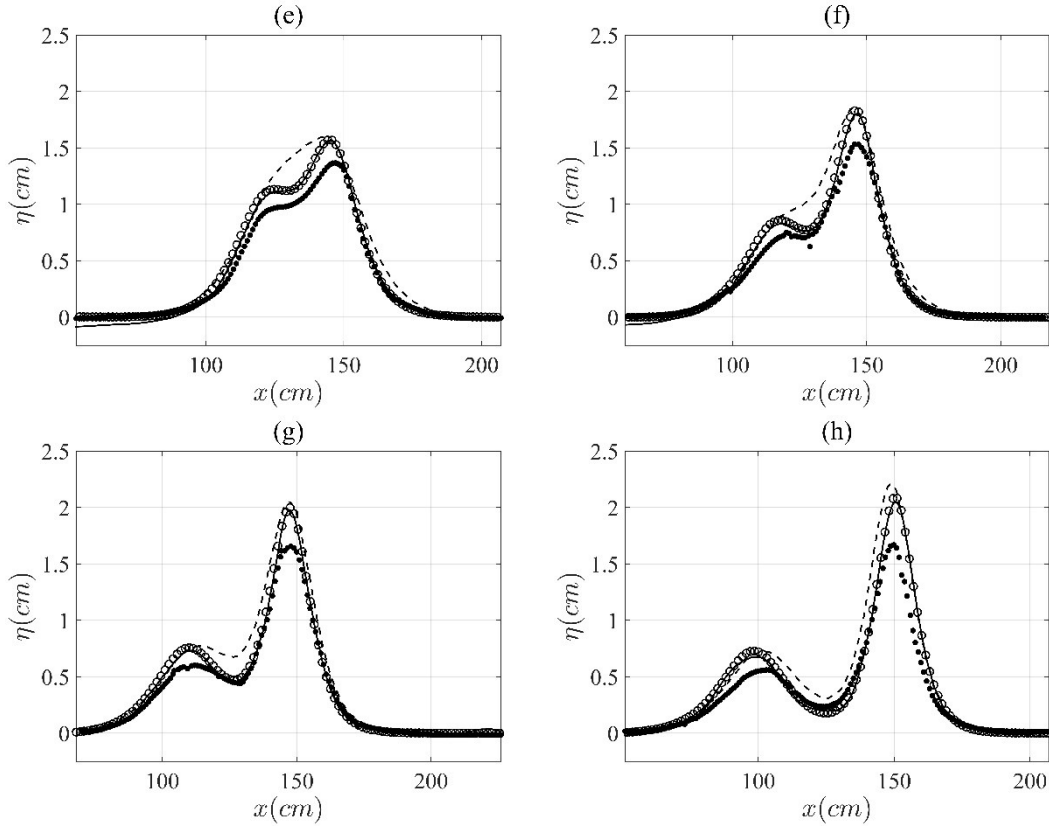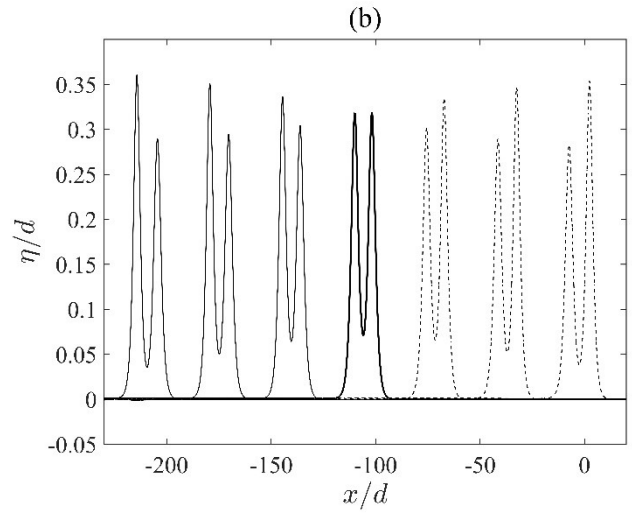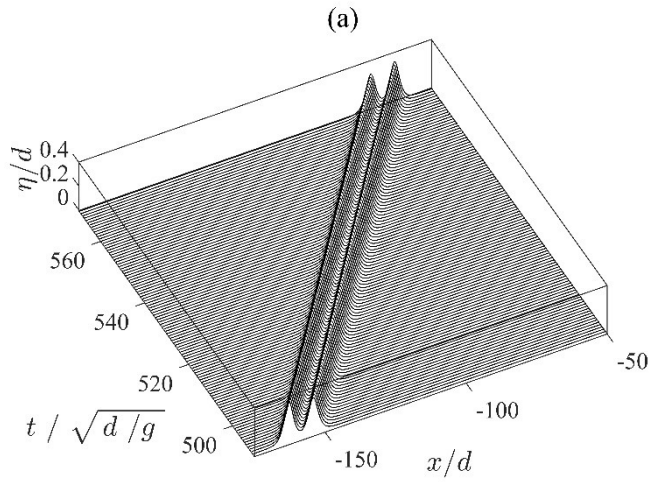
Figure 22. Overtaking collision of solitary waves with amplitudes A_1 = 2.295cm and A_2 =0.730cm at (a) t = 2.90304s, (b) t = 5.50196s, (c) t =6.40517s, (d) t = 7.05025s, (e) t = 7.60014s, (f) t = 8.50024s, (g) t = 9.50478s, (h) t = 11.30191s. Here，——，numerical result of Craig *et al.* [3]; - - - - - -, linear KdV solution; • • • • •, experimental result of Craig *et al.* [3]; ○, our present result.

      Figure. 22 shows a comparison of wave profiles among our present numerical result, the numerical and experimental result of Craig *et al.* [3] and the KdV two-soliton solution at different time. The quiescent water depth is d = 5.0cm. It can be observed that the present numerical result agree well with the numerical result of Craig *et al.* [3]. The overtaking process takes a long distance so that we can notice there is an obvious attenuation in the wave amplitudes due to the water viscosity in Craig *et al.*'s [3] experiment. Despite the wave amplitudes decrease with the distance, the wave profile still has the same form as numerical results at t = 7.05025s (**Figure. 22(d)**), while the linear KdV solution has already been unable to provide convincible prediction.

      Figure. 23 demonstrates a higher solitary wave of σ_1 = 0.4 catching up a smaller wave with amplitudes σ_2 = 0.3, 0.133, 0.113 and 0.1, respectively. Since the wave velocity is dependent on wave amplitude, the duration of the overtaking process is different from case to case. The length of the wave tank is much longer compared with head-on collision. In this study, the tank length has been adjusted to avoid wave reflection from the downsteam tank wall before the overtaking process is completed. The water depth is d = 1m in our simulations.

      It is difficult to tell from **Figure. 23(a)** whether the collision have happened or not, but we can identify the interaction from **Figure. 23(b)**. During the collision, the amplitude of the larger solitary wave monotonically decreases as the smaller wave rises up until the their amplitudes become identical at a critical time. After the critical time, the process reverses till two wave crests are well separated. Specifically, there are two distinguishable crests during the collision process. The whole interaction between solitary waves of σ_1 = 0.4 and σ_2 = 0.3 takes a very long CPU time as the relative velocity of the two waves is too small. After the collision, the higher solitary wave shifts forward while the smaller one shifts backward. Our numerical results for this case with ratio σ_1 / σ_2 =1.333 matches with both the KdV category (a) by Lax [28] and the category (a) by Craig *et al.* [3].
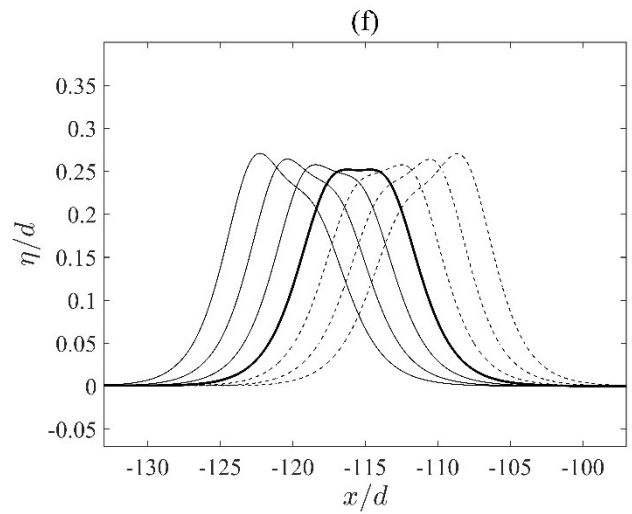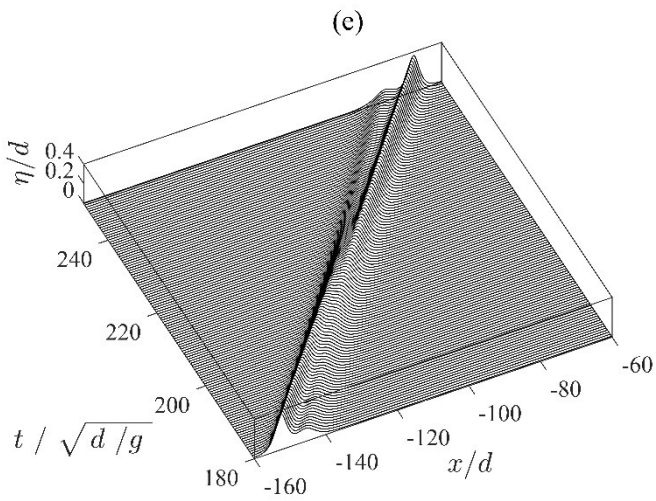
1

2

(a)

(b)

3

4

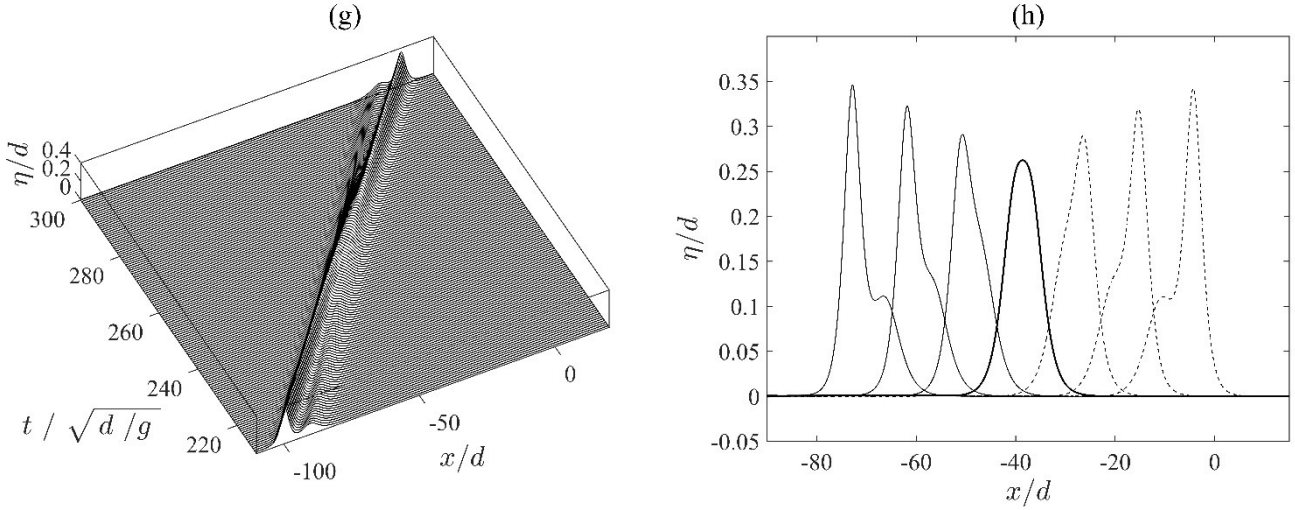5

(c)

(d)

6

7

8

(e)

(f)

9

23
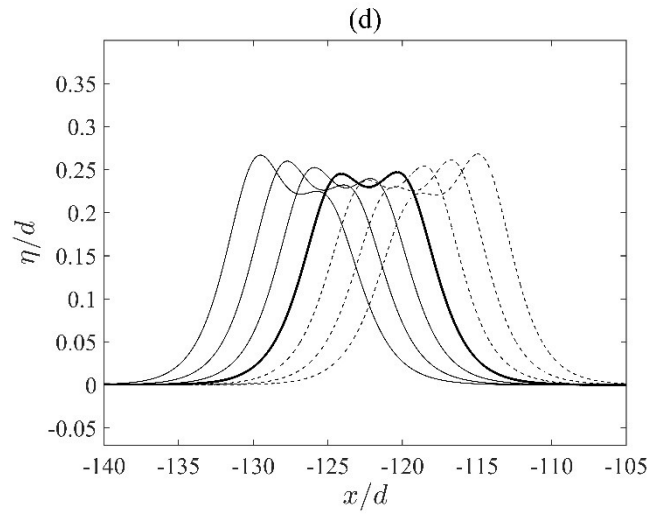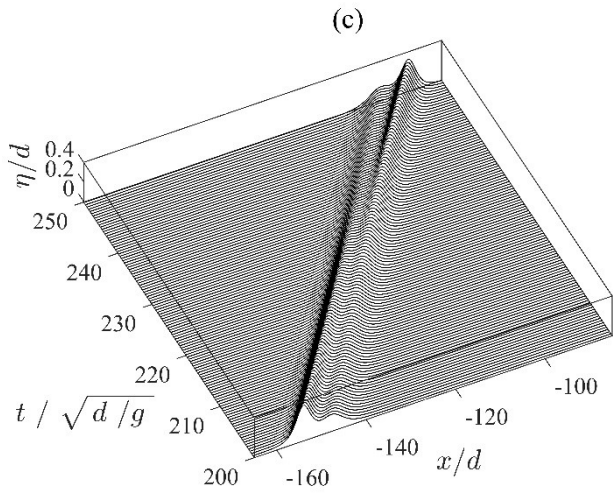
Figure 23. Overtaking collision for solitary waves of amplitudes: (a)-(b) for $\sigma_1 = 0.4$ and $\sigma_2 = 0.3$; (c)-(d) for $\sigma_1 = 0.4$ and $\sigma_2 = 0.1333$; (e)-(f) for $\sigma_1 = 0.4$ and $\sigma_2 = 0.113$ and (g)-(h) for $\sigma_1 = 0.4$ and $\sigma_2 = 0.1$. Each case shows both spatial-temporal plot (left) and wave profiles at different time (right) : ——— , the critical time when two waves exchange their relative positions; ——— , wave profile before the critical time ; --------, wave profile after the critical time.

For $\sigma_1 / \sigma_2 = 3$, shown in **Figure. 23(c) (d)** , the higher wave catches up with the smaller wave and then partially absorbs it. The dual-crest wave profile in our simulation at the critical time belongs to Lax's [28] category (a) though the distance between the two crests is significantly smaller than that in the first case with $\sigma_1 = 0.4$ and $\sigma_2 = 0.3$. But the amplitude ratio tells us that the result should have belonged to Lax's [28] category (b) or (c). So there is a conflict of our numerical result with the category of Lax [28].

Figure. 23(f) shows that there is a flattened peak instead of distinctive dual crests at the critical time for $\sigma_1 / \sigma_2 = 3.539$. The wave profile is supposed to be in the form of a single crest based on category (c) of Lax [28] at the critical time, while this ratio is defined as a critical transition value from category (b) to (c) in Craig *et al.* [3]. Our present numerical result for this case is essentially consistent with the revised category proposed by Craig *et al.* [3].

Figure. 23(h) shows only a single crest at the critical time for the case with $\sigma_1 = 0.4$ and $\sigma_2 = 0.1$. The larger wave gradually swallows the smaller one during the overtaking process. After the critical time, two waves re-emerge with a change of relative positions. This behaviour is the same as category (c) both in Lax [28] and Craig *et al.* [3].

Table 6: Spatial phase shifts and categary for overtaking collision of solitary waves

Case	σ_1	σ_2	σ_1/σ_2	Category in Lax [28]	Category in Craig *et al.* [3]	$\hat{s}_1$	$\hat{s}_2$	s_1	s_2
1	0.4	0.3	1.1333	a	a	5.7688	-6.3883	5.8896	-6.8007
2	0.4	0.1333	3	b or c	b	2.3666	-5.3963	2.9443	-5.1004
3	0.4	0.113	3.539	c	b or c	2.5960	-3.9291	2.6486	-4.9832
4	0.4	0.1	4	c	c	2.9604	-3.834	2.4566	-4.9131

Table 6 gives the theoretical and numerical result of the phase shifts as well as the category of the overtaking collision. $\hat{s}_1$ and $\hat{s}_2$ are the present numerical results and s_1 and s_2 represent theoretical results by **Eq. (21)**. It can be found that the numerical results agree well with analytical data.

5 Conclusions

A thorough analysis on the generation, propagation and interaction of solitary waves in a nonlinear numerical water wave tank based on the 2D Harmonic Polynomial Cell method is presented.

Four different methods of solitary wave generation are implemented in the numerical water wave tank. For $\sigma > 0.4$, the results by Goring's method are found to be less satisfactory because of reduction in amplitude and obvious trailing waves.

But the FNL method can produce solitary waves with minor trailing waves even for highly nonlinear waves.

For the head-on collision of solitary waves, our numerical results of the maximum run-up are in excellent agreement with the third-order approximation by Su & Mirie [1] up to $\sigma = 0.5$. For even higher waves, higher-order nonlinearity is not negligible so that the Su & Mirie's [1] theory fails to provide accurate prediction. But our fully-nonlinear numerical wave tank can still get the highly accurate results. Moreover, for the symmetric collision with $\sigma = 0.4$, our numerical results of wave profiles, phase shifts and the trailing waves after the collision are also successfully validated with experimental measurements of Chen & Yeh [2].

The phase shifts after the head-on collision are thoroughly investigated. Many researchers have questioned that Su & Mirie's [1] third-order prediction consistently underestimates the phase shifts when comparing with either their numerical results or experimental measurements. In present study, we demonstrate that the phase shift near to the collision center is larger than that far away from the collision domain. However, those researchers always mistakenly compared their immediate phase shifts with Su & Mirie's [1] third-order approximation of the uniform phase shifts. This is the main reason for the discrepancy. Additionally, inspired by Cooker et al. [26], we suggest to use the general 'fully interacting time' as the phase lag in time for both symmetric and asymmetric head-on collision. But the theoretical expression of the fully interacting time is not obtained, which could be a valuable research in the future work.

The overtaking collision of solitary waves is also studied for selected cases. Our numerical result is well validated with the numerical and experimental result of Craig et al. [3]. Furthermore, the simulations of four selected cases also strongly support Craig et al.'s [3] category of the overtaking collision process As for the phase shifts, our present results are also in good consistent with the analytical results by Li [51].

References

[1] C.H. Su, R.M. Mirie, On head-on collisions between two solitary waves, J. Fluid Mech. 98 (1980) 509–525. doi:10.1017/S0022112080000262.

[2] Y. Chen, H. Yeh, Laboratory experiments on counter-propagating collisions of solitary waves. Part 1. Wave interactions, J. Fluid Mech. 749 (2014) 577–596. doi:10.1017/jfm.2014.231.

[3] W. Craig, P. Guyenne, J. Hammack, D. Henderson, C. Sulem, Solitary water wave interactions, Phys. Fluids. 18 (2006) 1–25. doi:10.1063/1.2205916.

[4] J. Scott Russell, Report on Waves, in: Rep. Fourteenth Meet. Br. Assoc. Adv. Sci., 1844: pp. 311–390.

[5] J.L. Hammack, H. Segur, The Korteweg-de Vries equation and water waves. Part 2. Comparison with experiments, J. Fluid Mech. 65 (1974) 289–314. doi:10.1017/S002211207400139X.

[6] T. kishi and H. Saeki, the Shoaling, Breaking and Runup Op the Solitary Wave on Impermeable Rough Slopes, Coast. Eng. (1966) 322–347. doi:10.1007/978-94-6091-478-2_21.

[7] F.E. Camfield, R.L. Street, Shoaling of Solitary Waves on Small Slopes, J. Waterw. Harb. Div. 95 (1969) 1–22. http://cedb.asce.org/cgi/WWWdisplay.cgi?16167.

[8] D.G. Goring, Tsunamis: the propagation of long waves onto a shelf, 1979. Phd Thesis. California Institute of Technology, Pasadena, CA.

[9] G. Katell, B. Eric, Accuracy of solitary wave generation by a piston wave maker., J. Hydraul. Res. 40 (2002) 321–331. doi:10.1080/00221680209499946.

[10] S. Malek-Mohammadi, F. Testik, New methodology for laboratory generation of solitary waves, J. Waterw. Port, 136 (2010) 286–294. doi:10.1061/(ASCE)WW.1943-5460.0000046.

[11] N.J. Wu, S.C. Hsiao, H.H. Chen, R.Y. Yang, The study on solitary waves generated by a piston-type wave maker, Ocean Eng. 117 (2016) 114–129. doi:10.1016/j.oceaneng.2016.03.020.

[12] M.J. Boussinesq, Théorie de l'intumescence liquide, appelée onde solitaire ou de translation, se propageant dans un canal rectangulaire, C. R. Acad. Sci. Paris 72 (1871) 755–759

[13] C.E. Synolakis, The runup of solitary waves, J. Fluid Mech. 185 (1987) 523–545. doi:10.1017/S002211208700329X.

[14] J.D. Ramsden, Forces on a Vertical Wall due to Long Waves, Bores, and Dry-Bed Surges, J. Waterw. Port, Coastal, Ocean Eng. 122 (1996) 134–141. doi:10.1061/(ASCE)0733-950X(1996)122:3(134).

[15] A. Jensen, G.K. Pedersen, D.J. Wood, An experimental study of wave run-up at a steep beach, J. Fluid Mech. (2003) 161–188. doi:10.1017/S0022112003004543.

[16] S. Grilli, I.A. Svendsen, The propagation and runup of solitary waves on steep slopes, Rep. No. 91-4, Ctr. for Appl. Coast. Res., Univ. of Delaware, Newark, Del., 1991.

[17] L. Rayleigh, On waves, Phil. Mag. 1 (1876) 257–279.

[18] N.J. Wu, T.K. Tsay, Y.Y. Chen, Generation of stable solitary waves by a piston-type wave maker, Wave Motion. 51 (2014) 240–255. doi:10.1016/j.wavemoti.2013.07.005.

[19] J. Fenton, A ninth-order solution for the solitary wave, J. Fluid Mech. 53 (1972) 257–271. doi:10.1017/S002211207200014X.

[20] J.G.B. Byatt-Smith, An integral equation for unsteady surface waves and a comment on the Boussinesq equation, J. Fluid Mech. 49 (1971) 625–633. doi:10.1017/S0022112071002295.

[21] T. Maxworthy, Experiments on collisions between solitary waves, J. Fluid Mech. 76 (1976) 177–186. doi:10.1017/S0022112076003194.

[22] R.M. Mirie, C.H. Su, Collisions between two solitary waves. Part 2. A numerical study, J. Fluid Mech. 115 (1982) 475–492.

[23] J.D. Fenton, M.M. Rienecker, A Fourier method for solving nonlinear water wave problems: Application to solitary wave interactions, J. Fluid Mech. 118 (1982) 411–443.

[24] R.K.C. Chan, R.L. Street, A computer study of finite-amplitude water waves, J. Comput. Phys. 6 (1970) 68–94. doi:10.1016/0021-9991(70)90005-7.

[25] D.P. Renouard, F.J.S. Santos, A.M. Temperville, Experimental study of the generation, damping, and reflexion of a solitary wave, Dyn. Atmos. Ocean. 9 (1985) 341–358. doi:10.1016/0377-0265(85)90008-9.

[26] M. Cooker, P. Weidman, D. Bale, Reflection of a high-amplitude solitary wave at a vertical wall, J. Fluid Mech. 342 (1997) 141–158. doi:10.1017/S002211209700551X.

[27] Y. Chen, E. Zhang, H. Yeh, Laboratory experiments on counter-propagating collisions of solitary waves. Part 2. Flow field, J. Fluid Mech. 755 (2014) 463–484. doi:10.1017/jfm.2014.427.

[28] P.D. Lax, Integrals of nonlinear equations of evolution and solitary waves, Commun. Pure Appl. Math. 21 (1968) 467–490. doi:10.1002/cpa.3160210503.

[29] P.D. Weidman, T. Maxworthy, Experiments on strong interactions between solitary waves, J. Fluid Mech. 85 (1978) 417–431. doi:10.1017/S0022112078000713.

[30] N.J. Zabusky, M.D. Kruskal, Interaction of "solitons" in a collisionless plasma and the recurrence of initial states, Phys. Rev. Lett. 15 (1965) 240–243. doi:10.1103/PhysRevLett.15.240.

[31] C.S. Gardner, J.M. Greene, M.D. Kruskal, R.M. Miura, Method for solving the Korteweg-deVries equation, Phys. Rev. Lett. 19 (1967) 1095–1097. doi:10.1103/PhysRevLett.19.1095.

[32] R.L. Sachs, Completeness of derivatives of squared Schrödinger eigenfunctions and explicit solutions of the linearized KdV equation. SIAM Journal on Mathematical Analysis 14.4 (1983) 674-683.

[33] Q. Zou, C.H. Su, Overtaking collision between two solitary waves., PHYS. FLUIDS. 29 (1986) 2113–2123. doi:10.1063/1.865599.

[34] S.T. Grilli, J. Skourup, I.A. Svendsen, An efficient boundary element method for nonlinear water waves, Eng. Anal. Bound. Elem. 6.2 (1989) 97-107. doi:10.1016/0955-7997(89)90005-2.

[35] J.C. Harris, E. Dombre, M. Benoit, S.T. Grilli, Fast integral equation methods for fully nonlinear water wave modeling, in: Proc. Int. Offshore Polar Eng. Conf., 2014.

[36] Y.-L. Shao, O.M. Faltinsen, Towards Efficient Fully-Nonlinear Potential-Flow Solvers in Marine Hydrodynamics, in: Vol. 4 Offshore Geotech. Ronald W. Yeung Honor. Symp. Offshore Sh. Hydrodyn., 2012: p. 369. doi:10.1115/OMAE2012-83319.

[37] Y.L. Shao, O.M. Faltinsen, A harmonic polynomial cell (HPC) method for 3D Laplace equation with application in marine hydrodynamics, J. Comput. Phys. 274 (2014) 312–332. doi:10.1016/j.jcp.2014.06.021.

[38] A.G. Fredriksen, T. Kristiansen, O.M. Faltinsen, Experimental and numerical investigation of wave resonance in moonpools at low forward speed, Appl. Ocean Res. 47 (2014) 28–46. doi:10.1016/j.apor.2014.03.005.

[39] H. Liang, O.M. Faltinsen, Y.L. Shao, Application of a 2D harmonic polynomial cell (HPC) method to singular flows and lifting problems, Appl. Ocean Res. 53 (2015) 75–90. doi:10.1016/j.apor.2015.07.011.

[40] W. Zhu, M. Greco, Y. Shao, Improved HPC method for nonlinear wave tank, Int. J. Nav. Archit. Ocean Eng. 9 (2017). doi:10.1016/j.ijnaoe.2017.03.009.

[41] F.C.W. Hanssen, A. Bardazzi, C. Lugni, M. Greco, Free-surface tracking in 2D with the harmonic polynomial cell method: Two alternative strategies, Int. J. Numer. Methods Eng. 113 (2018) 311–351. doi:10.1002/nme.5615.

[42] S. Ma, F.C.W. Hanssen, M.A. Siddiqui, M. Greco, O.M. Faltinsen, Local and global properties of the harmonic polynomial cell method: In-depth analysis in two dimensions, Int. J. Numer. Methods Eng. 113 (2018) 681–718. doi:10.1002/nme.5631.

[43] A. Bardazzi, C. Lugni, M. Antuono, O.M. Faltinsen, Generalized HPC method for the Poisson equation. J. Comput. & Phys, 299 (2015) 630-648. doi.org/10.1016/j.jcp.2015.07.026.

[44] J. Wang, O.M. Faltinsen, A harmonic polynomial method based on Cartesian grids with local refinement for complex wave-body interactions. http://www.iwwwfb.org/workshops/33.htm/, 2018.

[45] F.-C.W. Hanssen, M. Greco, Y. Shao, The Harmonic Polynomial Cell Method for Moving Bodies Immersed in a Cartesian Background Grid, in: Vol. 11 Prof. Robert F. Beck Honor. Symp. Mar. Hydrodyn., 2015. doi:10.1115/OMAE2015-41282.

[46] M. Greco, A two-dimensional study of green-water loading, 2001. Phd Thesis. Norwegian University of Science and Technology

[47] R. Grimshaw, The solitary wave in water of variable depth. Part 2, J. Fluid Mech. 46 (1971) 611–622. doi:10.1017/S0022112071000739.

[48] D. Clamond, D. Dutykh, Fast accurate computation of the fully nonlinear solitary surface gravity waves, Comput. & Fluids. 84 (2013) 35–38. doi:10.1016/j.compfluid.2013.05.010.

[49] G. He, M. Kashiwagi, Numerical analysis of the hydroelastic behavior of a vertical plate due to solitary waves, J. Mar. Sci. Technol. (2012). doi:10.1007/s00773-011-0155-9.

[50] R.C. Ertekin, M. Hayatdavoodi, J.W. Kim, On some solitary and cnoidal wave diffraction solutions of the Green-Naghdi equations, Appl. Ocean Res. (2014). doi:10.1016/j.apor.2014.04.005.

[51] W. Li, Amplification of Solitary Waves along a Vertical Wall, 2012. Phd Thesis. Oregon State University